AD-A033 064 ROCKWELL INTERNATIONAL THOUSAND OAKS CALIF SCIENCE --ETC F/G 20/5
1.06 MICROMETER APD/LOW NOISE PREAMPLIFIER.(U)
JUN 76 I DEYHIMY, K NAKANO, R C EDEN F33615-75-C-1165
UNCLASSIFIED SC5019.7FR AFAL-TR-76-113 NL

| OF |
AD
A033064

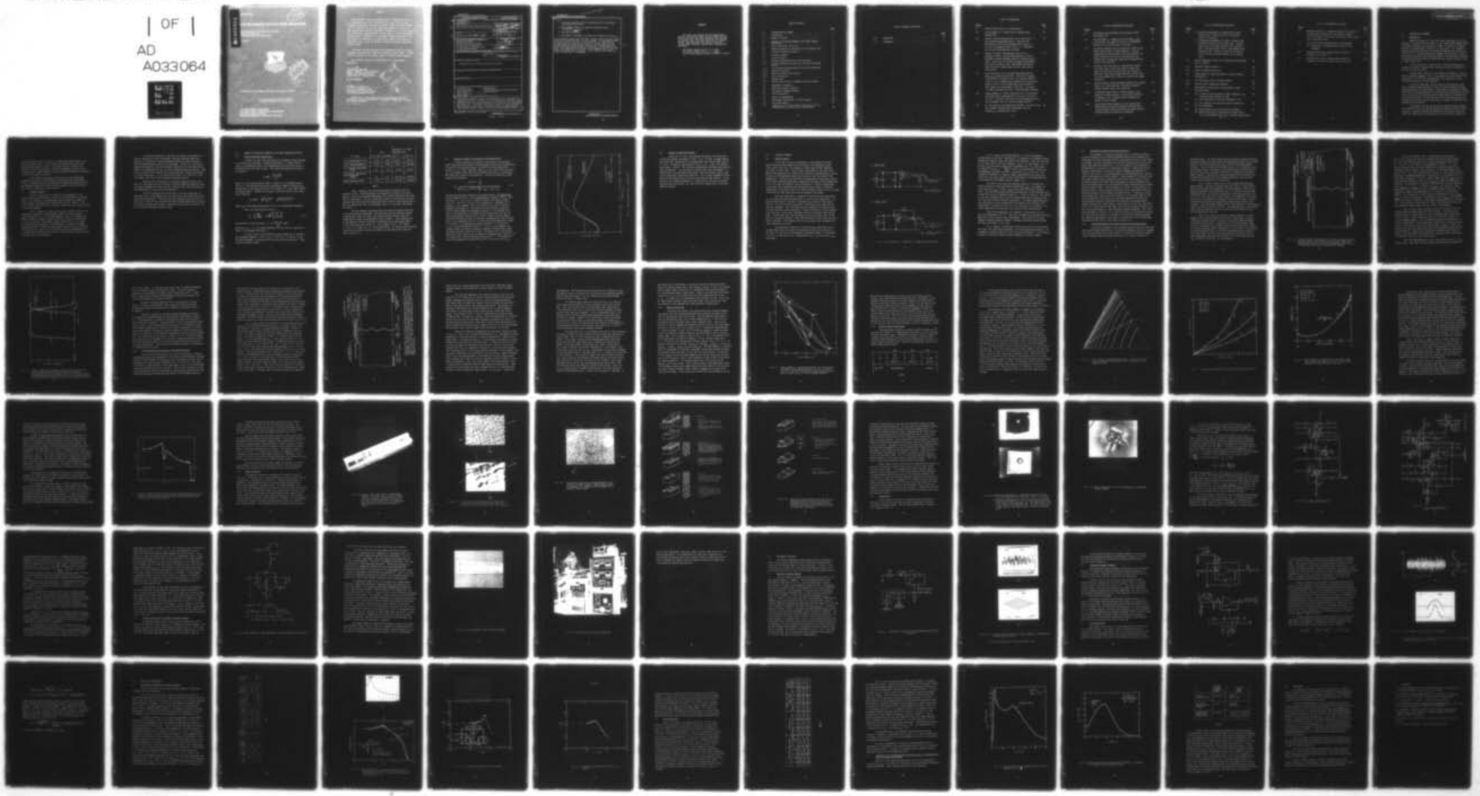

END
DATE
FILMED
2-77

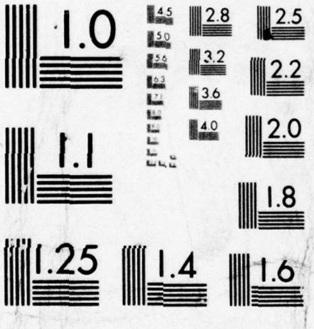
1.0
4.5
5.0
5.6
6.3
2.8
3.2
3.6
4.0
2.5
2.2
2.0
1.1
1.8
1.25
1.4
1.6

MICROCOPY RESOLUTION TEST CHART
NATIONAL BUREAU OF STANDARDS-1963-A

AD A033064

12

AFAL-TR-76-113

1.06 MICROMETER APD/LOW NOISE PREAMPLIFIER

SCIENCE CENTER, ROCKWELL INTERNATIONAL
1049 CAMINO DOS RIOS
THOUSAND OAKS, CALIFORNIA 91360

JUNE 1976

D D C
DEC 7 1976
C

FINAL REPORT FOR PERIOD 16 JANUARY 1975 through 30 JUNE 1975

Approved for public release; distribution unlimited

AIR FORCE AVIONICS LABORATORY
AIR FORCE WRIGHT AERONAUTICAL LABORATORIES
AIR FORCE SYSTEMS COMMAND
WRIGHT-PATTERSON AIR FORCE BASE, OHIO 45433

NOTICE

When Government drawings, specifications, or other data are used for any purpose other than in connection with a definitely related Government procurement operation, the United States Government thereby incurs no responsibility nor any obligation whatsoever; and the fact that the government may have formulated, furnished, or in any way supplied the said drawings, specifications, or other data, is not to be regarded by implication or otherwise as in any manner licensing the holder or any other person or corporation, or conveying any rights or permission to manufacture, use, or sell any patented invention that may in any way be related thereto.

This report has been reviewed by the Information Office (OI) and is releasable to the National Technical Information Service (NTIS). At NTIS, it will be available to the general public, including foreign nations.

This technical report has been reviewed and is approved for publication.

Donald J. Peacock

DONALD J. PEACOCK, Project Engineer
Electro-Optic Detectors Group
Electro-Optics Technology Branch

FOR THE COMMANDER

William C. Schoonover

WILLIAM C. SCHOONOVER, Chief
Electro-Optics Technology Branch
Electronic Technology Division

ACCESSION for
NTIS White Section ☑
DDC Buff Section ☐
UNANNOUNCED ☐
JUSTIFICATION ....
BY ....
DISTRIBUTION/AVAILABILITY CODES
Dist. AVAIL. and/or SPECIAL
A

Copies of this report should not be returned unless return is required by security considerations, contractual obligations, or notice on a specific document.

AIR FORCE - 22 NOVEMBER 76 - 100

UNCLASSIFIED
SECURITY CLASSIFICATION OF THIS PAGE (When Data Entered)

⑲ REPORT DOCUMENTATION PAGE

READ INSTRUCTIONS
BEFORE COMPLETING FORM

⑱ 1. REPORT NUMBER
AFAL-TR-76-113 ✓

2. GOVT ACCESSION NO.

3. RECIPIENT'S CATALOG NUMBER

4. TITLE (and Subtitle)
⑥ 1.06 Micrometer APD/Low Noise Preamplifier.

5. TYPE OF REPORT & PERIOD COVERED
⑨ FINAL REPORT. 16 Jan[redacted]-
1975 thru 30 Jun[redacted]75,

6. PERFORMING ORG. REPORT NUMBER
⑭ SC5019.7FR

7. AUTHOR(s)
⑩ I. Deyhimy, K. Nakano [redacted] R. C. Eden

8. CONTRACT OR GRANT NUMBER(s)
⑮ F33615-75-C-1165 New

9. PERFORMING ORGANIZATION NAME AND ADDRESS
Science Center, Rockwell International ✓
1049 Camino Dos Rios
Thousand Oaks, California 91360

10. PROGRAM ELEMENT, PROJECT, TASK AREA & WORK UNIT NUMBERS
⑯ Project No. 2001

11. CONTROLLING OFFICE NAME AND ADDRESS
Air Force Avionics Laboratory (DHO)
Air Force Systems Command
Wright-Patterson Air Force Base, Ohio 45433

12. REPORT DATE
⑪ Jun[redacted]976

13. NUMBER OF PAGES
79

14. MONITORING AGENCY NAME & ADDRESS (if different from Controlling Office)
⑫ 82 p.

15. SECURITY CLASS. (of this report)
UNCLASSIFIED

15a. DECLASSIFICATION/DOWNGRADING SCHEDULE

16. DISTRIBUTION STATEMENT (of this Report)

Approved for public release; distribution unlimited.

17. DISTRIBUTION STATEMENT (of the abstract entered in Block 20, if different from Report)

62204F

18. SUPPLEMENTARY NOTES

19. KEY WORDS (Continue on reverse side if necessary and identify by block number)

1.06μ Nd-YAG Laser	Heterojunctions
Avalanche Photodiode	III-V Alloy Microwave Avalanche Photodiode
Optical Receiver	Low Noise Preamp
Laser Communication	
Laser Imaging	

micrometers approx.

20. ABSTRACT (Continue on reverse side if necessary and identify by block number)

In this report, the design, fabrication and evaluation of a high sensitivity 1.06μ optical receiver is reported. This receiver utilizes a high-speed, high quantum efficiency III-V alloy heterojunction photodiode with very low junction capacitance (≃0.3 pf) hybrid integrated with a low-current noise transimpedance type preamplifier. The receiver is designed to operate in the 0-5 MHz band. These receivers have been shown to be the most sensitive wideband detectors of 1.06μ radiation to date. The work reported here entailed several distinct →

DD FORM 1 JAN 73 1473 EDITION OF 1 NOV 65 IS OBSOLETE

UNCLASSIFIED
SECURITY CLASSIFICATION OF THIS PAGE (When Data Entered)

389 949

mt

10 to the -15th power

efforts:

1) Liquid phase epitaxial growth of photodiode material, photodiode fabrication and evaluation.

2) Fabrication of extemely low capacitance feedback resistor $(C \leq 1\times10^{-15}F)$.

or =

3) Fabrication of receiver.

4) Development of measurement techniques and evaluation of receivers.

A total of three receivers were fabricated. The most sensitive receiver had an average NEP of 9.2×10^{-14} $W/\sqrt{Hz}$ in a 1 MHz bandwidth. In a bandwidth of 5 MHz, in order to achieve a RMS signal to RMS noise ratio of 3, with a 40% peak modulated signal, this same receiver requires an incident power of 4.4 nW. These detectors were operated without avalanche gain. With improvements in material technology, making possible an avalanche gain of about 20, and with a better first stage device in the preamp, a S/N of between 4 and 5 with a 1 nW incident light power level is possible. Further support of this program to achieve the above goals is recommended.

END

FOREWORD

This report was preapred by the Science Center, Rockwell International under contract F33615-75-C-1165. This report covers the period 16 January 1975 through 30 June 1975 and is the Final Report on this contract. The work described herein was carried out by the Science Center, Rockwell International, Thousand Oaks, California.

The project engineer was Dr. R. C. Eden.
The program manager was Dr. A. S. Joseph.
The Air Force contract monitor is Donald J. Peacock.

TABLE OF CONTENTS

Page

1.0 INTRODUCTION AND SUMMARY 1
1.1 Introduction 1
1.2 Summary of Results 2
2.0 ANALYSIS OF DETECTION PROBLEMS IN THE NIGHT IMAGING APPLICATION 4
2.1 Signal Shot-Noise Limited Case 4
2.2 Detection Problems in the Region of Low Avalanche Gain . . . 6
2.3 Summary of Detection Analysis. 8
3.0 TECHNICAL APPROACH 9
3.1 Receiver Design. 9
3.2 Avalanche Photodiode Design and Fabrication. 12
3.2.1 Inverted Heterojunction Microwave Avalanche Photodiode Design 12
3.2.2 The Inverted Homo-Heterojunction Avalanche Photodiode. . . . 17
3.2.3 Materials Selection. 22
3.2.4 Materials Growth and Evaluation. 24
3.2.5 Device Fabrication 32
3.3 Preamp Design. 38
3.4 Design & Fabrication of Feedback Resistance Element. 45
4.0 MEASUREMENT TECHNIQUES 51
4.1 Open-Loop Frequency Response 51
4.2 Closed-Loop Frequency Response 54
4.3 Noise Measurements 54
5.0 RESULTS OF MEASUREMENTS. 59
5.1 Measurement and Analysis of Signal Response. 59
5.2 Noise Measurements 64
5.3 Comparison of III-V APD Receiver Sensitivity with S-1 Photomultiplier and with Silicon APD Receiver. 66

TABLE OF CONTENTS (Continued)

Page

6.0 CONCLUSION 70

7.0 REFERENCES 71

LIST OF ILLUSTRATIONS

Figure		Page
2.1	Signal-to-noise ratio vs. avalanche gain	7
3.1	Circuit models for a) Normal and b) Feedback-type preamplifiers	10
3.2	Original inverted heterojunction III-V alloy microwave avalanche photodiode design. Note that the peak electric field (high avalanche gain) region is at the p^+ (transparent buffer layer) - n^- (absorbing active layer) heterojunction interface	14
3.3	Example of spectral photoresponse which can be obtained in either inverted heterojunction or (fully depleted) inverted homo-heterojunction avalanche photodiode. While this illustrates narrowband photoresponse which can be obtained, usual experimental devices are made with wider response peaks and near 100% quantum efficiencies	16
3.4	Device structure for an inverted homo-heterojunction $GaAs_{1-x}Sb_x$ avalanche photodiode. Note that as opposed to the earlier structure of Fig. 2.5, the peak electric field is at a p-n homojunction produced during continuous growth of the n^- active (absorbing) layer by adding a small amount of p-type dopant to the melt. The device is normally operated with the n^- layer completely depleted	19
3.5	Energy bandgap vs. lattice constant for all of the binary and ternary alloy semiconductors of Al, Ga or In with P, As or Sb. The solid lines are for direct bandgap materials and the dashed lines for indirect bandgap materials	23
3.6	Ga rich region of the GaAsSb phase diagram. The solid lines are liquidus isotherms while the dashed lines are $GaAs_xSb_{(1-x)}$ isocomposition lines	26

LIST OF ILLUSTRATIONS (Continued)

Figure		Page
3.7	Experimental and calculated Sb distribution curves for GaAsSb solid	27
3.8	Energy bandgap vs. composition for the $GaAs_{(1-x)}Sb_x$ alloy system. The region $0.4<x<0.65$ is inaccessible because of a miscibility gap in the alloy	28
3.9	Sb profile obtained from X-ray emission on SEM for two GaAsSb layers grown on a GaAs substrate. The melt composition for each epitaxial layer was identical but growth conditions at the time the second melt was brought over the substrate caused the Sb concentration to dip at the interface	31
3.10	Graphite slider boat used for "doping drop" growths. Top slider (small insert with holes) is where the dopant is place and the quartz push rod is used to push this slider back to where the sets of holes line up and the dopant drops through into the melt to change the doping	33
3.11	Normarski phase contrast photomicrographs of the surface details of an APD structure. Note the alignment of surface features along <110> directions	34
3.12	Interference phase contrast photomicrograph of the surface of an APD structure. These surface features are between 1 and 2 fringes which corresponds to a height of 2700 to 5400Å	35
3.13	Device fabrication procedure for the inverted homo-heterojunction avalanche photodiode (starting with a 3-layer epitaxial growth structure and ending with the APD chips ready for mounting or packaging)	36

LIST OF ILLUSTRATIONS (Continued)

Figure		Page
3.14	a) Reflection photograph of a diode where the dark circular dot is the mesa outline and the metal contact in the center b) Transmission photograph of a diode is taken by the infrared microscope from the layer side. The dark square area is the metal contact on the substrate side. The large bright circle is the window on the substrate side. The dark circular dot is the outline of the mesa and metal contact to the contact layer	39
3.15	Hybrid integrated 0-5 MHz III-V heterojunction photodiode optical receiver	40
3.16	Schematic diagram receiver #1	42
3.17	Schematic diagram receiver #3	43
3.18	Signal model for single gate Mosfet in source follower configuration	46
3.19	Low capacitance cermet resistance element	48
3.20	Cermet resistor evaporation apparatus	49
4.1	Experimental configuration for measurement of open-loop gain-phase	52
4.2	(a) 8 cycles of two sine waves of equal frequency. One sine wave totally buried in noise (b) Cross-correlation of the two sine waves in (a)	53
4.3	(a) Test capacitor for measuring impulse response and (b) its calibration	55
4.4	(a) Noise output and its statistical distribution (b) Measured statistical distribution of output noise, its log superimposed with log of a Gaussian distribution	57

LIST OF ILLUSTRATIONS (Continued)

Figure		Page
5.1	Measured amplitude vs. frequency response for receiver #3 as determined by taking FFT of the impulse response. (a) Direct output of the DPO on linear axes and (b) corrected to logarithmic axes	61
5.2	(a) Circuit model showing peaking in the passband	62
	(b) Magnitude of transimpedance of Receiver #3 vs. frequency	63
5.3	Measured output noise voltage spectral density vs. frequency for receiver #3	67
5.4	Measured output noise voltage spectral density vs. frequency for receiver #1 with 5 MHz post filter	68

PRECEDING PAGE BLANK-NOT FILMED

1.0 INTRODUCTION AND SUMMARY

1.1 Introduction

Among the important Air Force laser system requirements of the next few years is the laser line-scan system. In this airborne night imaging system, a high power Cw YAG:Nd laser, operating at 1.064μ, is slaved to a telescope which has a wide-band optical receiver at its focal point. This assembly is scanned in a direction parallel to the ground and perpendicular to the motion of the aircraft. Thus the scanning laser together with the motion of the aircraft form a raster type scan of the ground below. The laser beam is modulated by the ground reflectivity and the return beam, when properly displayed, gives an image of the terrain.

In order to make this system practical with existing power levels attainable in suitable airborne lasers, extremely stringent requirements are placed on the optical receiver.

The RMS signal to RMS noise ratio needed is preferably 5:1 with 3:1 being the minimum acceptable. This is to be achieved with the incoming light signal being 1 nW (10^{-9} watt), 40% modulated, with a bandwidth of 5 MHz (DC-5 MHz) preferred and 3.5 MHz acceptable.

As will be shown later, the only detector technology which comes close to meeting these requirements is the III-V alloy heterojunction photodiodes developed at the Science Center. These detectors represent the highest sensitivity in wide-band detection of 1.06μ radiation achieved anywhere to date. This is due to the fact that these devices convert photons to electrons with near ideal efficiency ($\eta = 0.95$), have very low noise of their own and, due to their extremely small junction capacitance, are capable of detecting light modulated at up to ten GHz.

The purpose of the present work was to design and develop preamplifiers capable of fully utilizing the performance advantages offered by these detectors. Commercial wide-band 50Ω preamps are not the best choice since their input capacitance and high Johnson noise current severely degrade the system performance. What is required is a preamp with extremely small equivalent input capacitance (~ 0.3 pf) and very low Johnson noise current from the photocurrent sensing resistor. In fact the only way in which a high sensitivity receiver can be built is by hybrid-integrating all the critical components onto a single substrate, with small dimensions between the components to reduce stray capacitive effects.

Three receivers were built in which the III-V alloy photodiodes were mated to low noise, low capacitance silicon Mosfet input stage preamplifiers. Of these the first two utilized hybrid integrated input sections with the subsequent stages consisting of discrete components, while the third was fully hybrid integrated on a single substrate.

1.2 Summary of Results

Thus far, in the first six months of this development, all our results have been obtained without the benefit of avalanche gain in the photodiode. In the regime of no avalanche gain, the best that can be hoped for is for the receiver performance to be Johnson-noise limited. Indeed, if there were no preamp noise contribution, a signal-to-noise ratio of 4 could be achieved in the 5 MHz bandwidth.

As it is, however, our best receiver, which is within 3 dB of being Johnson-noise limited in a 1 MHz bandwidth, requires 4.4 nW to achieve a signal-to-noise ratio of 3 in the 5 MHz bandwidth. Even in the reduced bandwidth of 3.5 MHz, to achieve a signal-to-noise ratio of 3, an incident power of 3.3 nW is required. These numbers reflect the fact that in this regime of operation (no avalanche gain), the performance is limited by the preamp noise contributions. In fact, with the present state of the art in electronic amplifying devices suitable for this application, without avalanche gain, it is unlikely that a signal-to-noise ratio of 5 can be achieved in the 5 MHz bandwidth with any receiver technology.

It should be pointed out, that while the results cited above fall short of meeting the system requirements, they were obtained without the benefit of avalanche gain, and nevertheless represent the best performance that has been achieved to date by any technology. In fact, our receiver was compared experimentally with the two other alternatives for this application, namely a S-1 photomultiplier and a silicon avalanche photodiode receiver. Both the S-1 and the silicon receiver were selected devices, representing products of mature technologies. Yet our receiver was better, by a factor of 2, than its closest rival, the silicon avalanche photodiode receiver.

That the III-V APD receiver is a promising approach becomes clear, when it is recognized that the relatively favorable comparison came after only six months development on these receivers, and that the silicon APD receiver, even theoretically, cannot meet the system goals.

The III-V heterojunction APD receiver is the only technology in a reasonable state of development which can satisfy this and other similar stringent system requirements. These receivers and conceptually similar ones delivered by us under Air Force (F33615-74-C-1030) and NASA (NAS5-23134) contracts for satellite communication systems represent the most sensitive detectors for 1.06μ radiation developed anywhere to date.

2.0 ANALYSIS OF DETECTION PROBLEMS IN THE NIGHT IMAGING APPLICATION

2.1 Signal Shot-Noise Limited Case

Consider the ideal case applicable to the problem of night imaging in a laser line scan system. Ultimate performance, i.e. signal-to-noise ratio, is achieved when there is no background and the only noise source is the shot-noise on the signal itself. The signal photo-generated current Is is given by,

$$I_s \text{ (RMS)} = \frac{m\eta \left(P_L / h\nu\right)}{\sqrt{2}}$$

where P_L is the received optical power, in watts, $h\nu$ is the photon energy in eV, η is the quantum efficiency of the detector (number of electrons per photon) and m is the modulation index of the signal (i.e. peak signal divided by minimum signal). The RMS noise current is the shot noise on this signal, and is given by,

$$I_{ns} \text{ (RMS)} = \sqrt{2q\, I_{DC}\, \Delta F} = \sqrt{2q\, (\eta\, P_L / h\nu)\, \Delta F} \quad ,$$

where I_{DC} is the average photocurrent, and ΔF is the measurement bandwidth.

Thus, the signal-to-noise ratio is:

$$\frac{S}{N} = \frac{I_s \text{ (RMS)}}{I_{ns} \text{ (RMS)}} = \frac{m}{2} \sqrt{\eta \left(\frac{P_L}{q\, h\nu\, \Delta F} \right)} \qquad (2.1)$$

Alternatively, solving for power: $P_L = \frac{1}{\eta} \; \frac{4q\, h\nu\, \Delta F}{(m)^2} \; (S/N)^2$.

Note that m, P_L, ν, ΔF are system parameters and that the only detector parameter is the quantum efficiency, η.

In order to get a better feeling for the problem, let us consider a few reasonable examples. Let m = 0.4, $P_L = 10^{-9}$ W, $h\nu = 1.165$ eV. We can use these parameters to calculate S/N for various existing detectors. These results are shown in Table 1.

	S/N		Required P_L in 5 MHz Bandwidth for:	
η (1.06μ)	ΔF=3.5 MHz	ΔF=5 MHz	S/N = 3	S/N = 5
(S-1 Photocathode) $\eta=0.1\%$	0.25	0.20	210 nW	585 nW
(III-V Photocathode) $\eta=1\%$	0.78	0.65	21 nW	58.5 nW
(Si Avalanche Photodiode) $\eta=15\%$	3.2	2.75	1.4 nW	3.9 nW
(III-V Alloy - Heterojunction Photodiode) $\eta=95\%$	7.6	6.3	0.22 nW	0.615 nW
(Ideal Detector) $\eta=100\%$	7.82	6.5	0.21 nW	0.585 nW

TABLE 1

Table 1 represents the limiting performance attainable with the detectors listed. The photocathodes are immediately eliminated from consideration. The silicon avalanche photodiode, while ideally performs in the right *order of magnitude*, is also not a good choice since in practice with its high avalanche gain noise and large capacitance (which leads to high preamp noise) it does not approach the ideal in performance, even if it had twice the quantum efficiency.

The only detector technology which has promise of meeting the goals is the heterojunction photodiode. Of course even with this detector without avalanche gain, there is no way, with existing state-of-the-art amplifier technology, to achieve the performance listed in Table 1. With avalanche gain in the detector, the only limitation to achieving the ultimate performance is the excess gain noise factor, X_n. As an example, for $P_L = 10^{-9}$ watts, $m = 0.4$, $\Delta F = 3.5$ MHz, $X_n = 0.1$, M (avalanche gain) = 20, and using the measured value for dark current in one of our diodes, we calculate an RMS signal-to-noise ratio of 4.3.

2.2 Detection Problems in the Region of Low Avalanche Gain

In order to analyze the situation in the region of low avalanche gains, where other noise sources are non-negligible, we must write an expression for the noise current which takes all the significant noise sources into account, i.e. $i_n = \sqrt{i_{ns}^2 + i_{nj}^2 + i_{ne}^2}$. Where i_{ns} is the total shot-noise current, i_{nj} is the Johnson current noise of the load-resistor, and i_{ne} is the equivalent input noise current of the preamplifier. Writing this explicitly in the signal-to-noise equation:

$$\frac{S}{N} = \frac{(m/\sqrt{2}) \quad M \quad \frac{\eta P_L}{h\nu}}{\sqrt{2q\, \Delta F\, [I_s + M^{(2+X_n)} (\frac{\eta P_L}{h\nu} + I_B)] + i_{nj}{}^2 + i_{ne}{}^2}}, \tag{2.2}$$

The terms not previously defined are the avalanche gain M, the unmultiplied surface leakage current I_s, and the multiplied bulk leakage current I_B. Note that when $I_s = 0$, $I_B = 0$, $X_n = 0$, then for large M, this equation reduces to Eq. (1). Fig. 2.2.1 is a plot of this equation for a reasonable set of parameters. For M between 1 and 2, the signal-to-noise ratio is actually degraded as photodiode bias is increased since the attendant surface dark current increase swamps the advantage of the gain, M. For M between 2 and about 10, the performance is controlled by the avalanche gain and (S/N) increases approximately linearly with M. As M is further increased, however, the excess multiplication term (X_n) dominates and degrades the signal-to-noise ratio. Also, noteworthy in Fig. 2.1 is that unless an avalanche gain of about 4 is possible, it is preferable to operate with gain of 1, since S/N for $1 < M \leq 4$ is actually worse than for $M = 1$. At $M = 1$, with reasonably low leakage currents, the noise is essentially composed of Johnson noise current and preamp equivalent input noise current. The Johnson noise is minimized by choosing as large a load-resistor as bandwidth requirements permit (see Sec. 3), and represents the limiting performance possible at $M = 1$. The preamplifier noise simply degrades the signal-to-noise ratio from the limit set by i_{nj}.

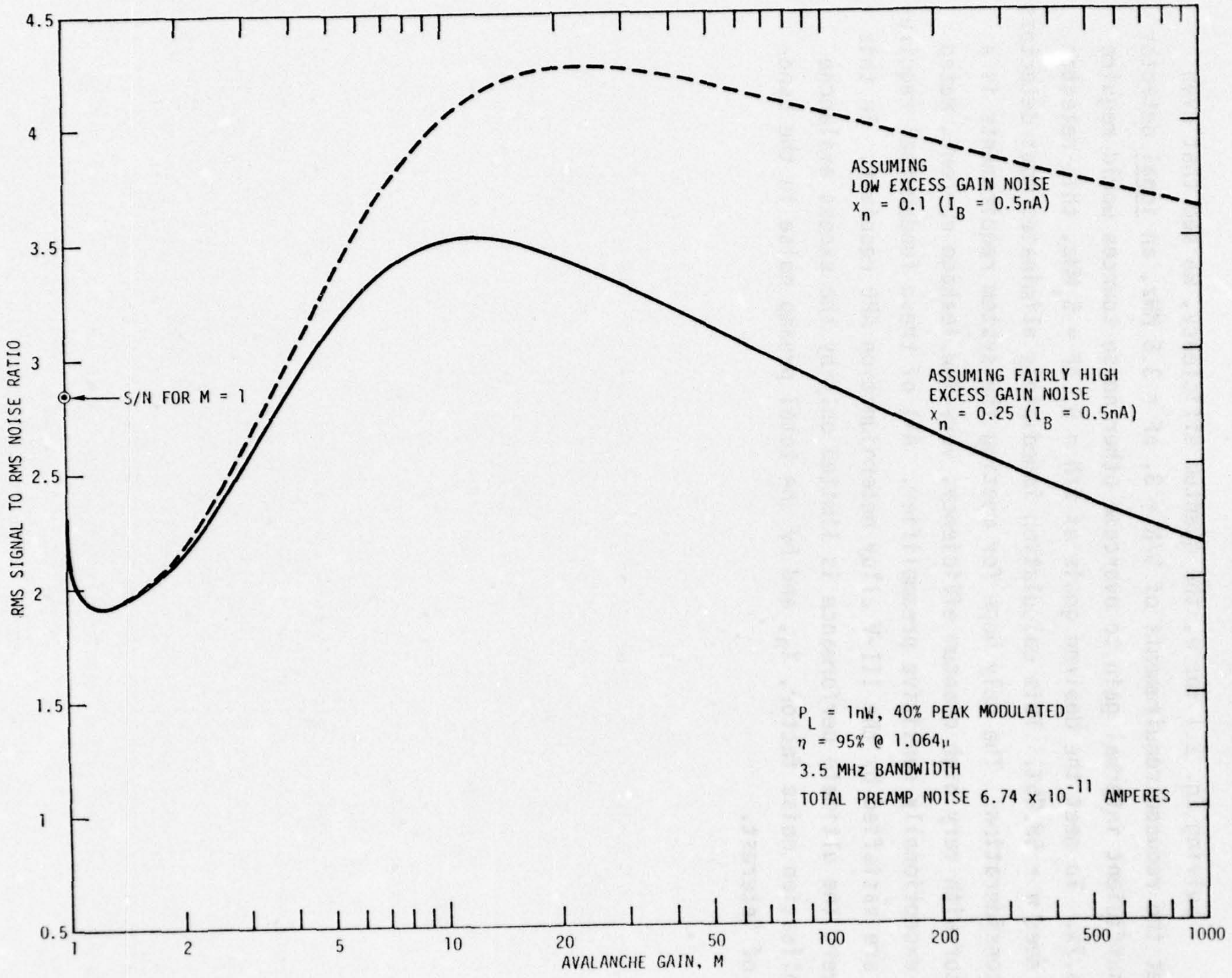

Fig. 2.1 Signal-to-noise ratio vs. avalanche gain

2.3 Summary of Detection Analysis

Solving Eq. 2.1 for η, the quantum efficiency, we see that even to meet the reduced requirements of $S/N = 3$, $\Delta F = 3.5$ MHz, an ideal detector with sufficient internal gain to overcome other noise sources would require $\eta = 14.7\%$. To meet the desired goals of $S/N = 5$, $\Delta F = 5$ MHz, this detector would need $\eta = 58.25\%$. This calculation immediately eliminates most detectors from consideration. The only hope for meeting the system requirements is a detector with very high quantum efficiency, very low leakage current, mated to an exceptionally sensitive preamplifier. All of these fundamental requirements are satisfied by the III-V alloy heterojunction APD receiver. In this receiver, the ultimate performance is limited only by the excess avalanche multiplication noise factor, X_n, and by the total preamp noise in the bandwidth of interest.

3.0 TECHNICAL APPROACH

3.1 Receiver Design

In the ideal receiver a photodiode of unity quantum efficiency would be used and the preamplifier would convert the photodiode current into a useful high level, low impedance voltage signal without degrading the signal-to-noise ratio. The principal contributions to the total noise made by the preamplifier are Johnson noise current of the photocurrent sensing resistor and the equivalent input noise current of the first stage of the preamplifier. The key factor determining the magnitude of these noise sources is the total equivalent capacitance appearing at the input of the preamplifier. This is so, since the amplifier noise contribution is directly proportional to the total input capacitance and the Johnson noise current is inversely proportional to the square root of the load resistance, which in turn is limited in value by the input capacitance and the bandwidth requirement.

The input capacitance is composed of the APD junction capacitance, C_j, the equivalent amplifier capacitance C_{in} and the stray capacitance. The junction capacitance of the APD is minimized by the design of that device (see Sec. 3.2) and the stray capacitance is minimized by the layout of the receiver components. The equivalent amplifier capacitance is determined by the input amplifier device capacitance. Bipolar Transistors are not suitable since they have a large input capacitance and also relatively large current noise. Junction Fets also have relatively high input current noise, so the choice is narrowed to Mosfets. These devices, while not ideal, offer the best choice available. The RF Mosfets used in our receivers have reasonably low input capacitance and noise.

The conventional approach for converting the photocurrent into a voltage signal would be to sense the photocurrent with a load resistor at the input of a low-noise, high-impedance, high-speed preamp. As illustrated in Fig. 3.1 a) the value of R_L is determined by $(C_j + C_{in})$ and by the f_{-3dB} requirement.

a) NORMAL PREAMP

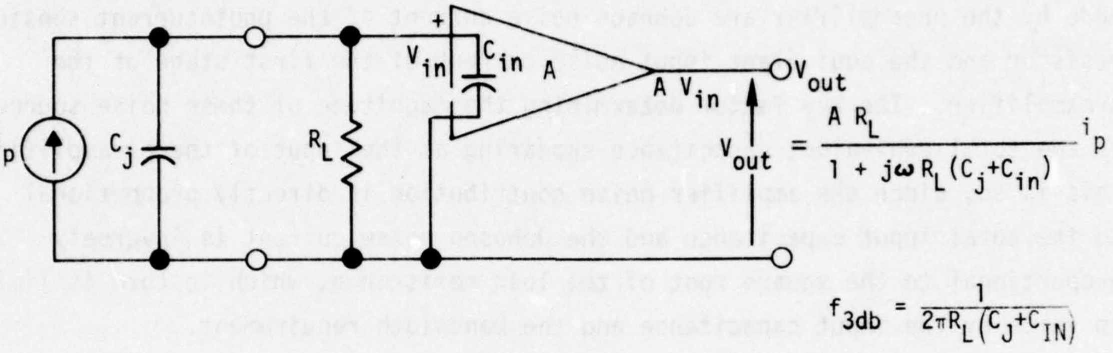
+
V_in
C_in
A
A V_in
V_out
i_p
C_j
R_L
V_out

$$V_{out} = \frac{A R_L}{1 + j\omega R_L (C_j + C_{in})} i_p$$

$$f_{3db} = \frac{1}{2\pi R_L (C_J + C_{IN})}$$

b) FEEDBACK PREAMP

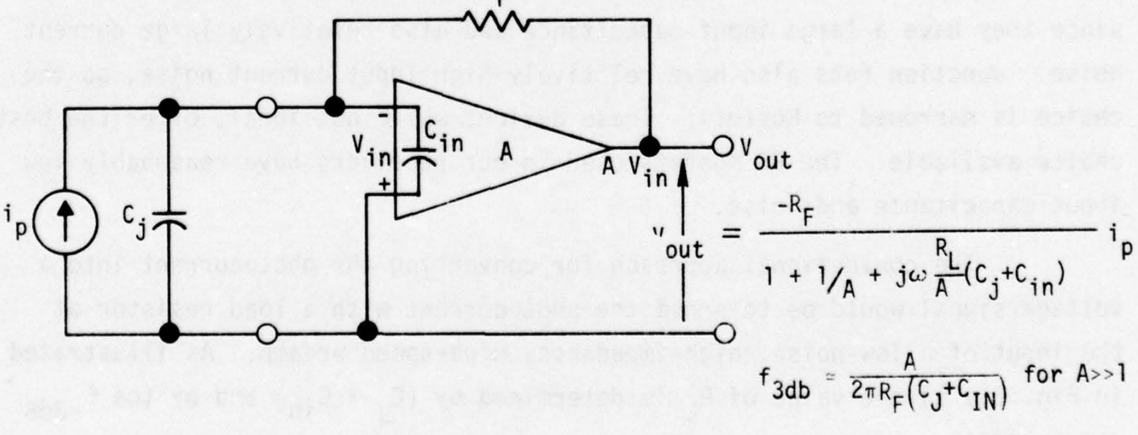
R_F
-
V_in
C_in
+
A
A V_in
V
out
i_p
C_j

$$V_{out} = \frac{-R_F}{1 + 1/A + j\omega \frac{R_L}{A}(C_j + C_{in})} i_p$$

$$f_{3db} = \frac{A}{2\pi R_F (C_J + C_{IN})} \text{ for } A >> 1$$

Fig. 3.1 Circuit models for a) Normal and b) Feedback-type preamplifiers.

Fig. 3.1 shows an alternate approach, i.e. the transimpedance configuration in which the "load-resistor" is connected as a feedback resistor between the inverting input, and output of the amplifier. Here, for the same set of values used in the first approach, f_{-3dB} is 'A' times higher. So, if we keep f_{-3dB} the same as before, this allows the use of 'A' times larger R_L ($R_F = AR_L$). Since $i_{nj} = \frac{4kT\,\Delta F}{R_L}$ and for this application $A \simeq 400$, this transimpedance connection results in a reduction in i_{nj} of $\sqrt{A} \simeq 20$. This feedback configuration is, however, highly susceptible to oscillation and instability, and places rather critical restrictions on the characteristics of the amplifier and feedback resistor element, R_F.

Any poles in the open-loop frequency response of the amplifier itself must be well above the required closed-loop f_{-3dB}. For example, if the closed-loop f_{-3dB} is 5 MHz, f_{-3dB} for the amplifier should be beyond 8 MHz. Note that this coupled with the open-loop gain of about 400 means that an amplifier with gain-bandwidth product of > 3.2 GHz is required. The resistor R_F must have extremely small stray distributed capacitance to ground as well as a very small effective shunting capacitance. The former capacitance would cause phase-shift in this element which when added to the 90° phase shift accumulated at the input due to R_F $(C_i + C_j)$ could lead to oscillation. The latter capacitance has to be small as this $R_F C_F$ limits the bandwidth.

These stray capacitances are required, in this system, to be no more than approximately 10^{-15} F. There are no commercially available resistors, known to us, which can meet these requirements. The success of the transimpedance approach depends on whether a feedback resistance element meeting the above requirements is available.

So, in summary, the optimized receiver would utilize a high quantum efficiency, low capacitance photodiode, a low input capacitance amplifier, and a feedback resistance element with very low stray capacitance.[1] The following sections of "Technical Approach" address themselves to these problems.

3.2 Avalanche Photodiode Design and Fabrication

The ultimate in receiver performance will be attained by combining a low noise preamp with an avalanche photodiode (APD) having extremely low capacitance (for high charge sensitivity), high quantum efficiency (near 100%), low leakage, low series resistance and sufficient avalanche gain to raise the signal level above the preamp noise. The first question to be addressed in the APD design is the choice of semiconductor material. Because the optical absorption coefficient in silicon (an indirect bandgap semiconductor) at 1.064μ is only 10 cm^{-1}, silicon photodiodes at this wavelength have a serious transit time-quantum efficiency tradeoff. Direct-bandgap III-V alloys, on the other hand, exhibit optical absorption coefficients on the order of 10^4 cm^{-1} for photon energies just above their energy gaps, so that photodiodes fabricated from these materials can simultaneously exhibit high quantum efficiencies and short transit times. The next question to resolve is the selection of a device structure. After examining the design goals we developed a radically different approach to the avalanche photodiode design. In addition to being the structure most likely to be able to meet all of the design goals for the system application, this detector has the added advantages of allowing a very convenient mounting configuration and providing a narrowband optical response characteristic which makes it sensitive only to the 1.06μ laser radiation. Our initial work on these APD's used a device structure referred to as the inverted heterojunction 1.06μ microwave avalanche photodiode. This structure, described in Section 3.2.1 is used for the APD in the delivered receiver. Our later work has involved a refinement of this original approach designed for improved avalanche gain characteristics referred to as the inverted homo-heterojunction APD, which is described in Section 3.2.2.

3.2.1 Inverted Heterojunction Microwave Avalanche Photodiode Design

In the device approach to the avalanche photodiode detector described here, sophisticated heteroepitaxial fabrication techniques using III-V compound and alloy semiconductors are used in order to circumvent the design tradeoffs (such as between speed and quantum efficiency, etc.) usually entailed in photodiode design. The inverted heterojunction microwave avalanche photodiode structure introduces the light through the transparent substrate into the three-layer III-V alloy (principally $GaAs_{1-x}Sb_x$ alloys have been used) detector structure. The use of substrate and alloys with $E_g > h\nu$ as transparent, very low resistance contacts and optical filters makes possible a device with very low series resistance, high quantum efficiency and controllable narrowband optical response. These factors, along with the mesa device structure, give a device with extremely wide signal bandwidth capability, low noise (dark current) and the capability for avalanche gain.

Fig. 3.2 shows a drawing of the 1.06μ microwave avalanche photodiode structure. The device structure shown starts with a p^+ GaAs substrate and has alloy compositions selected for 1.06μ peak response. We have also fabricated devices of the complimentary type (i.e. starting with n-type GaAs substrate material) and with alloy compositions giving peak responses in the 0.9 to 1.15μ range (with wider ranges possible). The substrate in this structure serves as a transparent low resistance contact to the device, as well as the physical mounting base and hermetically sealing optical window to the "outside". The light entrance window portion of the substrate is anti-reflection coated to minimize reflective light loss. The substrate doping is sufficiently high to give low resistance, but not so high as to cause significant free carrier absorption of the light.

The p^+ alloy buffer layer grown on the GaAs substrate is a direct bandgap III-V alloy with composition such that its energy gap is slightly larger than the photon energy of interest (1.165 eV for 1.064μ wavelength). This means that this layer is transparent at the desired wavelength (hence acting as a transparent low resistance contact to the junction) but, because of the sharp absorption edge of the material, acts as a cutoff filter defining the short wavelength (high hν) cutoff of the photodiode spectral response. This buffer layer also serves to minimize the lattice mismatch with the n^- active (absorbing) layer over what it would be if it were a GaAs substrate (E_g = 1.4 eV) to n^- alloy (E_g = 1.1 eV) interface.

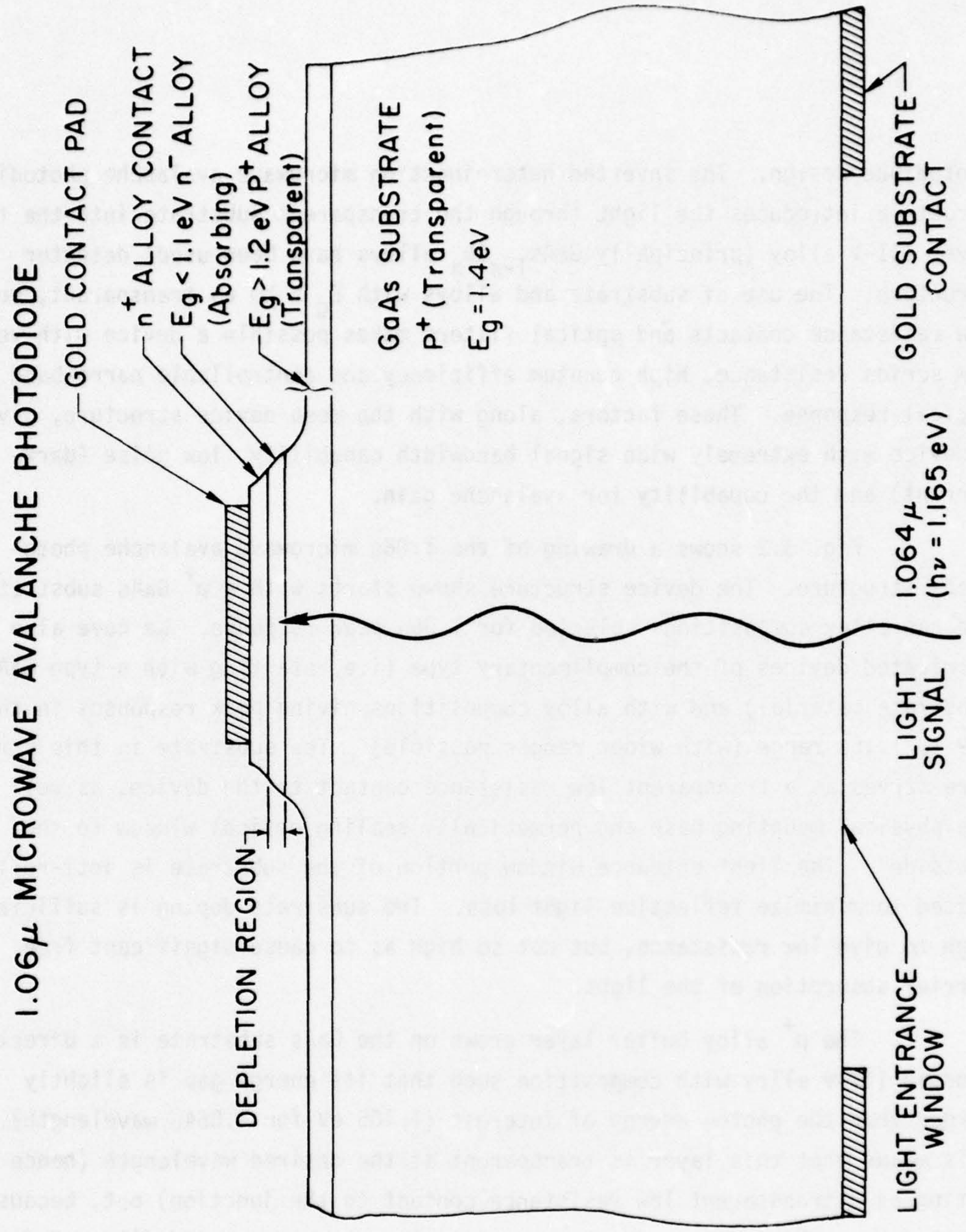
1.06μ MICROWAVE AVALANCHE PHOTODIODE
GOLD CONTACT PAD
n+ ALLOY CONTACT
Eg < 1.1 eV n− ALLOY
(Absorbing)
Eg > 1.2 eV P+ ALLOY
(Transparent)
GaAs SUBSTRATE
p+ (Transparent)
Eg = 1.4eV
DEPLETION REGION
GOLD SUBSTRATE CONTACT
1.064 μ
(hν = 1.165 eV)
LIGHT SIGNAL
LIGHT ENTRANCE WINDOW

Fig. 3.2. Original inverted heterojunction III-V alloy microwave avalanche photodiode design. Note that the peak electric field (high avalanche gain) region is at the p^+ (transparent buffer layer) - n^- (absorbing active layer) heterojunction interface.

On top of the buffer layer is heteroepitaxially grown the n^- alloy "active" layer with energy gap somewhat less than the photon energy ($E_g < h\nu$), such that the material has a very high absorption coefficient ($\alpha \sim 10^4$ cm^{-1}) for the light of the wavelength of interest. It is the absorption edge of this layer which defines the long-wavelength cutoff of the spectral photoresponse of the photodiode, i.e. the layer becomes transparent for $h\nu < E_g$. This combined buffer layer-active layer cutoff action for producing a narrowband photoresponse characteristic is illustrated in Fig. 3.2. Here actual transmission curves for a typical GaAs substrate (T_{GaAs}) and a 10μ thick epitaxial $GaAs_xSb_{1-x}$ alloy film (T_{buffer}) are shown (corrected for reflection). For purposes of illustration, the absorption curve for the active layer, $A_{active} = 1-T_{active}$, is taken as $1-T_{buffer}$, only shifted to longer wavelength slightly (since the active layer has a smaller energy gap). The quantum efficiency versus wavelength for this structure is given by the product of the transmission of the device up to the depletion region (T_{GaAs} T_{buffer}) times the absorption in the depletion region (A_{active}; assuming the whole active layer is depleted). This product photoresponse curve, as shown in Fig. 3.3 can be quite narrow (260Å full width at half height) yet have high peak quantum efficiency (about 82% near 1.064μ in the example).

This n^- active layer is depleted from the p-n junction near the interface with the buffer layer well into the layer. The width of the depletion region is determined by the bias voltage and donor concentration in the n^- layer. Typical values for W for $N_d \approx 10^{16}$ cm^{-3} are about 3.2μ with a breakdown voltage ~ 70 volts applied (avalanche gain operation). In certain circumstances it may be desirable to deplete all of the way through this n^- active layer to the n^+ alloy contact layer, whereas in other cases depletion only part way through the layer may be preferable (both types have been fabricated). These various conditions of depletion layer width and electric field distribution are obtained by varying the donor concentration and thickness for this n^- alloy active layer.

The final heteroepitaxial layer in the structure is the n^+ alloy contact layer. This layer is heavily doped to provide an ohmic contact for

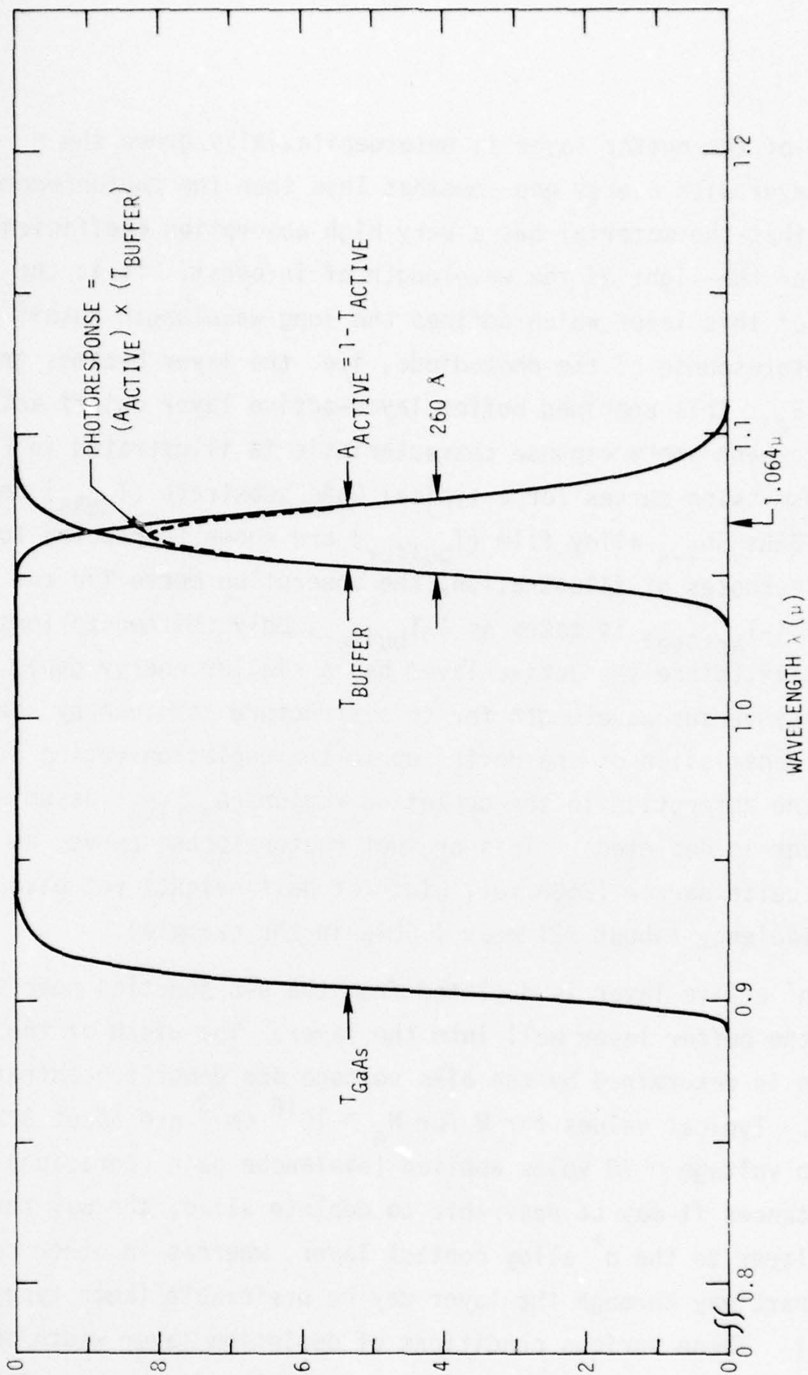

Fig. 3.3. Example of spectral photoresponse which can be obtained in either inverted heterojunction or (fully depleted) inverted homo-heterojunction avalanche photodiode. While this illustrates narrow-band photoresponse which can be obtained, usual experimental devices are made with wider response peaks and near 100% quantum efficiencies.

the n^- active layer. In cases where the active layer is completely depleted it also defines the edge of the depletion region. The alloy content is adjusted to give the same (or slightly larger) energy gap as the n^- active layer so that optical transmission measurements may be used to monitor the active layer energy gap as a process control.

Because of the heavy doping of the p^+ substrate and n^+ contact layer, it is easy to alloy metallic ohmic contacts to these regions and to plate the contacts with thick gold for convenience in making contact to the devices.

The device structure is defined by photolithography and etching of the mesa to the required shape and side contours as described in Section 3.5. The angled sides of the mesa at the depletion layer are an essential part of the device structure. The peak electric field in the depletion region occurs at the p-n junction toward the substrate side of the depletion region. If no special precautions were taken at the surface, concentration of electric field at the edges of the junction would be expected to lead to surface breakdown before the center of the junction area began to give significant avalanche gain. By sloping the junction edges, as shown in Fig. 3.2 by careful etching, the electric field at the edges of the junction is reduced significantly below the values toward the center of the device and hence the device may be used for avalanche operation. The surface may be operated exposed, or covered with a suitable passivation layer.

3.2.2 The Inverted Homo-Heterojunction Avalanche Photodiode

In the initial work on these III-V alloy 1.06μ detectors, inverted heterojunction $GaAs_{1-x}Sb_x$ photodiodes of the type just described were developed which had 1.064μ quantum efficiencies over 95%, low leakage currents, and low capacitances and transit times (bandwidths of dc to 15 GHz into a 50Ω load). In addition to single detectors, of the type shown in Fig. 3.2, two dimensional arrays were fabricated with this structure. The principal limitation in these earlier devices was that the high frequency avalanche gain attainable was very limited and the gain uniformity was poor because of microplasmas caused by heterojunction interface defects at the peak electric field point in the depletion region. Such problems might reasonably be expected in the structure of Fig. 3.2 because of the fact that at this p^+ buffer n^- active layer interface there will necessarily be both heterojunction lattice-mismatch defects (because the increased antimony composition in the active layer gives it a larger lattice constant than the buffer) and growth-nucleation non-uniformities caused by the interruption in the growth, when the buffer layer melt is removed and the active layer melt is rolled on to the growth surface. Because of the strong dependence of avalanche gain on local electric field or ionizable defects, any such non-uniformities or defects lead to local areas in the junction with reduced breakdown voltages. Such areas will undergo local microplasma breakdown, limiting the useful (low noise) APD reverse bias range to voltages below those required to achieve high avalanche gains over the bulk of the device.

Fig. 3.4 shows the device structure for an inverted homo-heterojunction $GaAs_{1-x}Sb_x$ 1.06μ avalanche photodiode designed to circumvent the gain limitations inherent in the earlier inverted heterojunction design. The device is fabricated by growing three liquid epitaxial layers of GaAsSb on a GaAs substrate. The light is brought into the device through the n^+ GaAs substrate, which is, of course, transparent at 1.064μ ($h\nu = 1.165$ eV) since the photon energy is less than the energy gap ($E_g = 1.4$ eV) and the n^+ doping is not so high as to cause significant "free carrier" (intraband-transistion) absorption. The n^+ $GaAs_{1-y}Sb_y$ ($y \sim 0.12$) "buffer" layer ($E_g \sim 1.2$ eV) is also transparent at 1.06μ, but it does serve to define the short wavelength cutoff of the detector, as well as to minimize the lattice mismatch at the buffer-active heterojunction. The active (absorbing) layer of $GaAs_{1-x}Sb_x$ ($x \sim 0.17$) is the unique feature of the homo-heterojunction device structure. Because its energy gap (~ 1.1 eV) is less than $h\nu$, the 1.06μ light is strongly absorbed in this layer, with most of the light absorbed within 1 or 2 microns of the active-buffer interface. The active layer is started in the liquid-epitaxial growth process as an n^- layer ($N_D \sim 1.5 \times 10^{15}$ cm^{-3}), but after about 3 to 5 microns of growth, p-type dopant is added to the melt so that a p-n homojunction is grown in this active layer. This means that the peak field region of the depletion

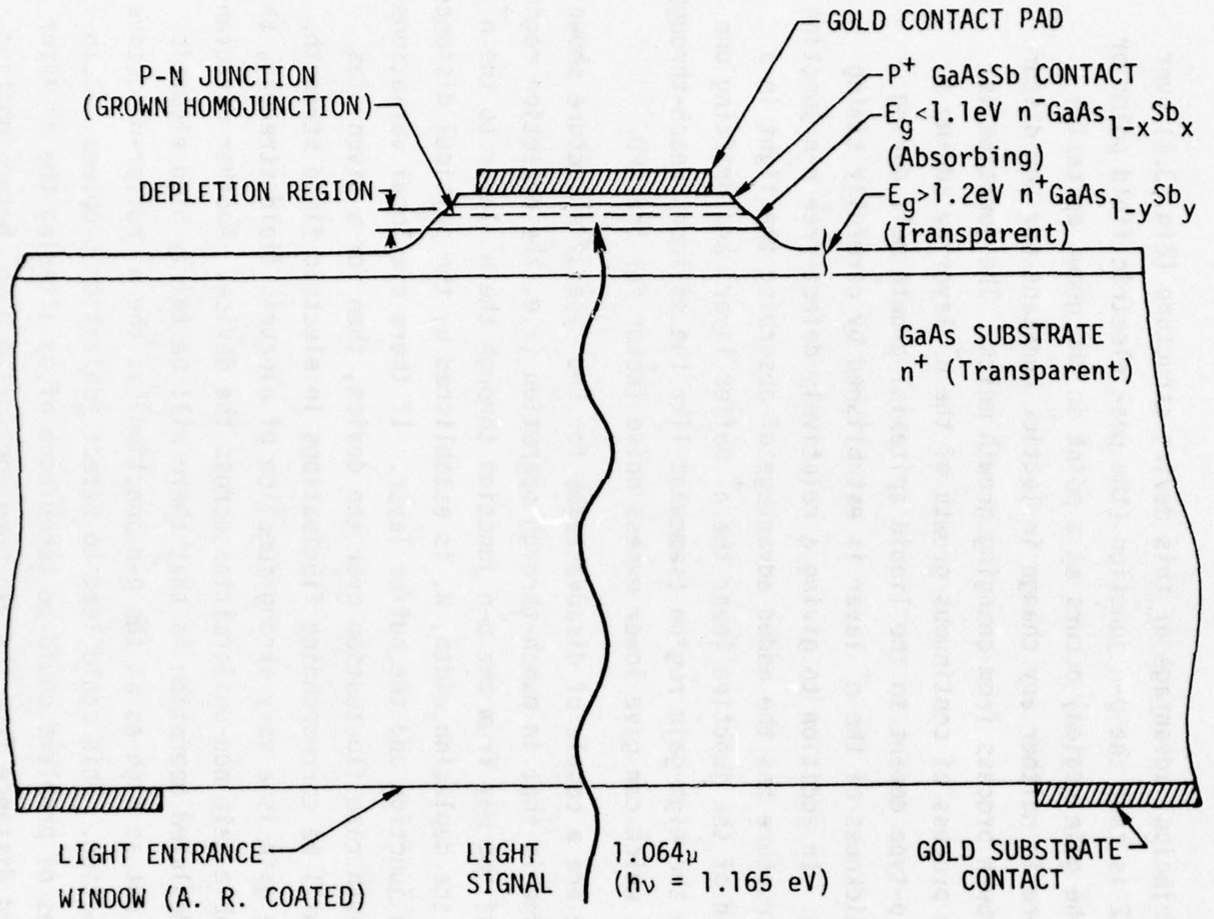
GOLD CONTACT PAD
P-N JUNCTION (GROWN HOMOJUNCTION)
P^+ GaAsSb CONTACT
E_g<1.1eV $n^-GaAs_{1-x}Sb_x$ (Absorbing)
DEPLETION REGION
E_g>1.2eV $n^+GaAs_{1-y}Sb_y$ (Transparent)
GaAs SUBSTRATE n^+ (Transparent)
LIGHT ENTRANCE WINDOW (A. R. COATED)
LIGHT SIGNAL
1.064μ (hν = 1.165 eV)
GOLD SUBSTRATE CONTACT

Fig. 3.4 Device Structure for an Inverted Homo-Heterojunction $GaAs_{1-x}Sb_x$ Avalanche Photodiode. Note that as opposed to the earlier structure of Fig. 2.5, the peak electric field is at a p-n homojunction produced during continuous growth of the n^- active (absorbing) layer by adding a small amount of p-type dopant to the melt. The device is normally operated with the n^- layer completely depleted.

region occurs at a grown homojunction free from either interlayer growth, interface defects or heterojunction (lattice mismatch or other) interface defects.

The principal advantage of this device structure (Fig. 3.4) over that of Fig. 3.2 is that the p-n junction (the peak electric field point or highest avalanche gain region) occurs at a point in the grown epitaxial layer where there is neither any change in lattice constant nor any disturbance in the growth process from changing growth melts. The junction is produced in the process of continuous growth of the n^- layer by adding a tiny amount of p-type dopant to the liquid epitaxial growth melt during growth. The thickness of the n^- layer is established by carefully timing the dopant drop. In addition to giving a relatively defect-free p-n junction region, this structure has the added advantage of absorbing the light in a low-field region of the junction (near the n^+ buffer layer) and drifting one carrier through the high-gain region (somewhat like the silicon "reach-through" APD structure), which can give lower excess noise factor for the APD.

There are a couple of disadvantages for the type of structure shown in Fig. 3.4. One is that in punch-through operation (i.e. the depletion region extending all of the way from the p-n junction through the n^- layer to the n^+ buffer layer), the depletion width, W, is established by the physical distance between the p-n junction and the buffer layer. If there are local variations in W due to growth rate fluctuation over the device, then for a given bias voltage there will be corresponding fluctuations in electric field strength. Since avalanche gain is a very strong function of electric field strength, this can cause sizeable gain non-uniformities across the device. Another disadvantage of fully depleted operation is that there will be fairly high electric fields (though not as high as at the p-n junction) at the n^+ buffer-n^- active layer heterojunction. This could lead to defect ionization problems. Both of these sources of problems could be taken care of by altering the n^- layer doping level and distance from the p-n homojunction to n^--n^+ heterojunction distance so that the depletion region almost - but not quite - reaches the heterojunction. This would require some minority carrier diffusion to reach the depletion region, of course, but if the thickness of undepleted absorbing material were small enough (~ 1μ), this should not significantly degrade quantum efficiency or response time.

An interesting point about the structure of Fig. 3.4 is that one would expect from the location of the p-n junction at the surface side of the n^- layer that with the slope of the mesa edges shown, there would be field concentration near the p-n junction at the device perimeter and hence surface (rather than bulk) breakdown. In fact, considerable effort at the beginning of this work was extended toward developing "upside down" mesas to avoid this problem. However, it was found that if surface passivations are used which tend to induce a p-type surface channel on the $GaAs_{1-x}Sb_x$ surface of the n^- layer, the channel effect works opposite to the geometrical field concentration effect so that devices of the type in Fig. 3.4 can be fabricated without giving surface breakdown problems.

The structure of Fig. 3.4 was adopted on the basis of GaAs ionization data which indicates that hole ionization rates are larger than electron ionization rates. Hence, in this structure the light is absorbed near the n^+ buffer n^- active layer interface and the photogenerated holes are drifted through the high field region (near the p-n junction) for avalanche gain. However, recent measurements on these $GaAs_{1-x}Sb_x$ alloys[2] indicate that in the x range of interest, the electron ionization rate is considerably larger than the hole ionization rate ($\alpha_n >> \alpha_p$). Measurements of gain versus wavelength on our experimental diodes of the type shown in Fig. 3.4 support this conclusion. In this structure, if (as originally assumed) holes had the higher ionization rate, then the shorter the wavelength, the higher would be the optical absorption coefficient for the light, the closer to the n^+ buffer-n^- active layer heterojunction the carriers would be generated and the more electric field the holes would get to pass through in transiting the junction. Hence, for $x_p >> x_n$, we would expect the highest avalanche gain at the short wavelength side of the photoresponse curve. In fact, just the opposite is observed. As the reverse bias on the diodes is increased, the gain increases much sooner toward the long wavelength side of the response, causing, in fact, the response peak at higher biases to shift out to a wavelength which would have been on the long wavelength edge at lower biases. Hence we conclude that the original assumption of $\alpha_p >> \alpha_n$ must be wrong for this alloy composition and in fact $\alpha_n >> \alpha_p$. This means that the complimentary APD structure (as Fig. 3.4 but with all doping types reversed) should give much higher, more uniform gains than were observed in the experimentally fabricated APD's reported here.

3.2.3 Materials Selection

The desired low leakage, high quantum efficiency and wide bandwidth requirements for this avalanche photodiode place extremely stringent limitations on the materials which can be used. The most important requirement is that the semiconductor must have a direct bandgap with $E_g \sim 1.16$ eV so that the photons are all absorbed within a small distance (2-3μ). There are no elemental or binary compound semiconductors which can satisfy this requirement, thus one is force to use a III-V ternary alloy. A diagram of energy bandgap vs. lattice constant is useful for this selection because it shows the useful alloys, the potential substrate materials and the degree of lattice mismatch between them. Such a diagram is shown in Fig. 3.5. All of the potential III-V alloy combinations are found by following a line of constant energy gap of $E_g = 1.16$ eV across the intersection with each ternary alloy in Fig. 3.5. The possible choices are as follows: $Ga_xIn_{1-x}As$, $GaAs_xSb_{1-x}$, $InAs_xP_{1-x}$, $In_xAl_{1-x}As$, GaP_xSb_{1-x}, InP_xSb_{1-x}, $Ga_xAl_{1-x}Sb$ and $In_xAl_{1-x}Sb$. The requirement of a substrate which is transparent at 1.06μ and a reasonable lattice match between substrate and epitaxial layer eliminates all but the first three choices. At the start of this program, InP was not grown domestically, and that which was available was of very low quality, thus it was eliminated in favor of GaAs as the choice for substrate material. Of the above three alloys, only $Ga_xIn_{1-x}As$ and $GaAs_xSb_{1-x}$ will grow on GaAs. Both of these ternaries have been grown successfully on GaAs and the choice between these two alloys reduces to the one which has fewer interface problems, better chemical homogeneity and fewer device fabrication problems. Since actual device fabrication and performance are the

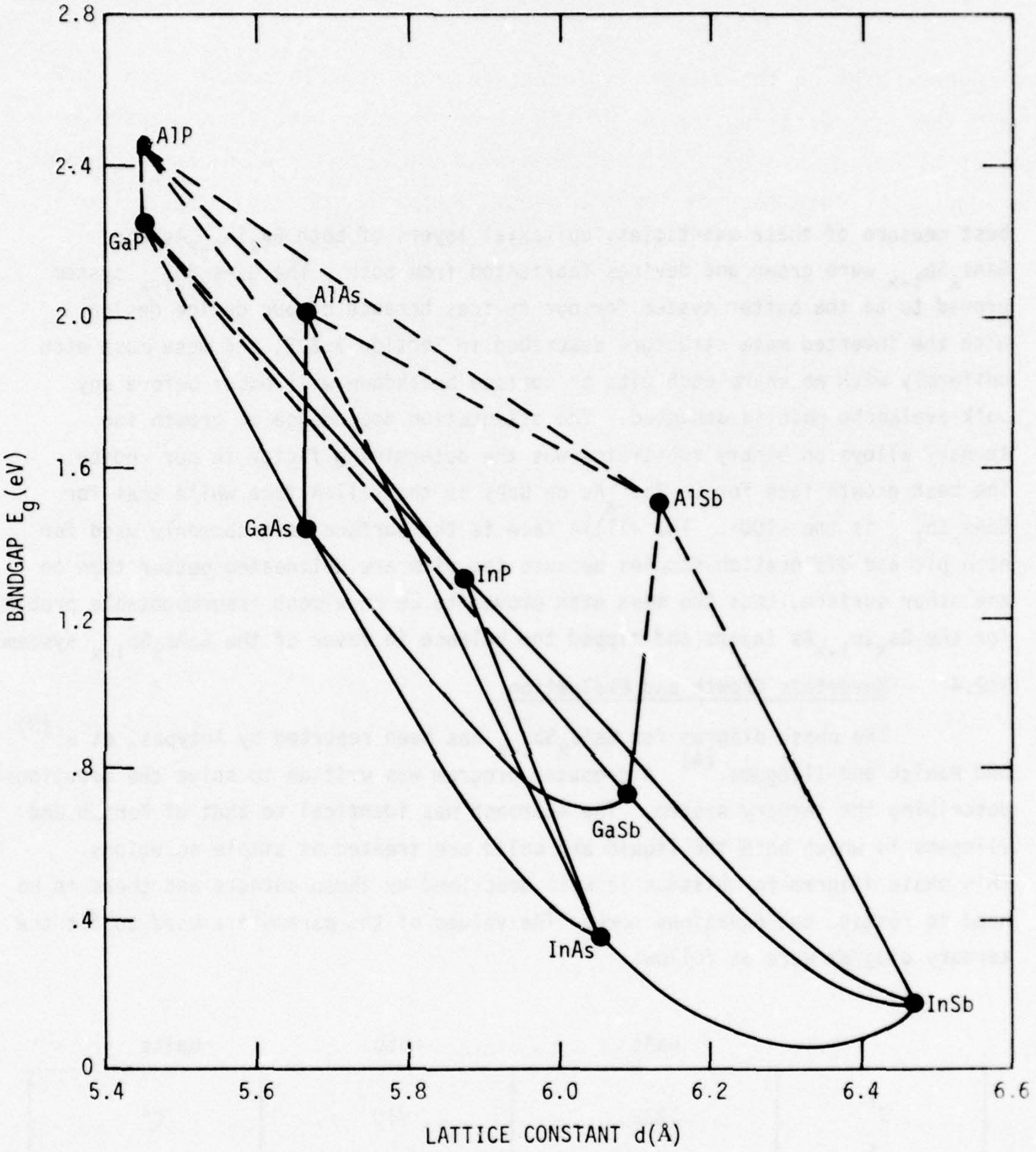

Fig. 3.5. Energy bandgap vs. lattice constant for all of the binary and ternary alloy semiconductors of Al, Ga or In with P, As or Sb. The solid lines are for direct bandgap materials and the dashed lines for indirect bandgap materials.

best measure of these quantities, epitaxial layers of both $Ga_xIn_{1-x}As$ and $GaAs_xSb_{1-x}$ were grown and devices fabricated from both. The $GaAs_xSb_{1-x}$ system proved to be the better system for our devices because of our device design. With the inverted mesa structure described in Section 3.2.2, the mesa must etch uniformly with no sharp etch pits or surface breakdown will occur before any bulk avalanche gain is achieved. The orientation dependence of growth for ternary alloys on binary substrates was the determining factor in our choice. The best growth face for $Ga_xIn_{1-x}As$ on GaAs is the <111>A face while that for $GaAs_xSb_{1-x}$ is the <100>. The <111>A face is the surface most commonly used for etch pit and dislocation studies because the pits are delineated better than on any other surface, thus the mesa etch proved to be an almost insurmountable problem for the $Ga_xIn_{1-x}As$ layers and tipped the balance in favor of the $GaAs_xSb_{1-x}$ system.

3.2.4 Materials Growth and Evaluation

The phase diagram for $GaAs_xSb_{1-x}$ has been reported by Antypas, et al(3) and Panish and Illegems.(4) A computer program was written to solve the equations describing the ternary system. The approach was identical to that of Panish and Illegems in which both the liquid and solid are treated as simple solutions. This phase diagram formulation is well described by these authors and there is no need to restate the equations here. The values of the parameters used to fit the ternary diagram were as follows:

	GaAs	GaSb	Units
T^F	1238	710	C°
ΔS^F	16.64	15.8	e.u./mole
α	5160-9.16T	4700-6.0T	cal/mole
$\alpha_{As-Sb}=750$	$\beta_{GaAs-GaSb}=2700$		cal/mole

TABLE 2

The calculated liquidus lines for the Ga rich corner are shown in Fig. 3.6 and calculated and experimental points for the coefficient of GaSb vs. Sb mole fraction in the melt with temperature as a parameter is shown in Fig. 3.7. This calculated phase diagram is in reasonable agreement with our experimental data on the composition of epitaxial layers and it has proven to be very useful to determine the melt composition and growth temperature to achieve the desired solid alloy compositions for the multiple layers in the APD.

From the data on the energy bandgap vs. composition for $GaAs_xSb_{1-x}$ in Fig. 3.8, a composition of ~ 16% GaSb (i.e. x = .84) is required for the active layer of the avalanche photodiode. In order to avoid Sb build up and compositional changes during growth it is desirable to grow the ternary in a region where the Sb mole fraction in the solid does not change rapidly with temperature. From Fig. 3.7, one observes that temperatures of 750°C or higher are required. We have elected to grow at 775°C with a ΔT of ~ 5°C during growth of the epitaxial layers. The increasing GaSb fraction with decreasing temperature is a desirable feature in our particular device structure because the buffer layer will tend to be graded to more closely match the active layer and reduce the number of edge dislocations at the interface. Since both p^+-n-n^+ and n^+-p-p^+ structures are required to study the electron and hole avalanche multiplication coefficients, both p^+ and n^+ GaAs substrates are required as well as either p or n doping for each of the three epitaxial layers. For p-type doping Zn, Ge and Si have been used and for n-type Sn and Te have been used. Ge, Si and Sn are particularly useful dopants if more than one epitaxial layer is grown at a time because they all have low vapor pressures and cause a minimum of cross contamination between the melts. These are the only dopants used in the APD structure because a lightly doped region with a moderately high breakdown voltage is always required and the high vapor pressure dopants would preclude the growth of this layer. As noted above, both n^+-p-p^+ and p^+-n-n^+ structures have been grown, however, for simplicity, further descriptions of the growth will refer only to the p^+-n-n^+ structure. For this structure, the buffer layer is Sn doped while both the active and contact layers are Ge doped.

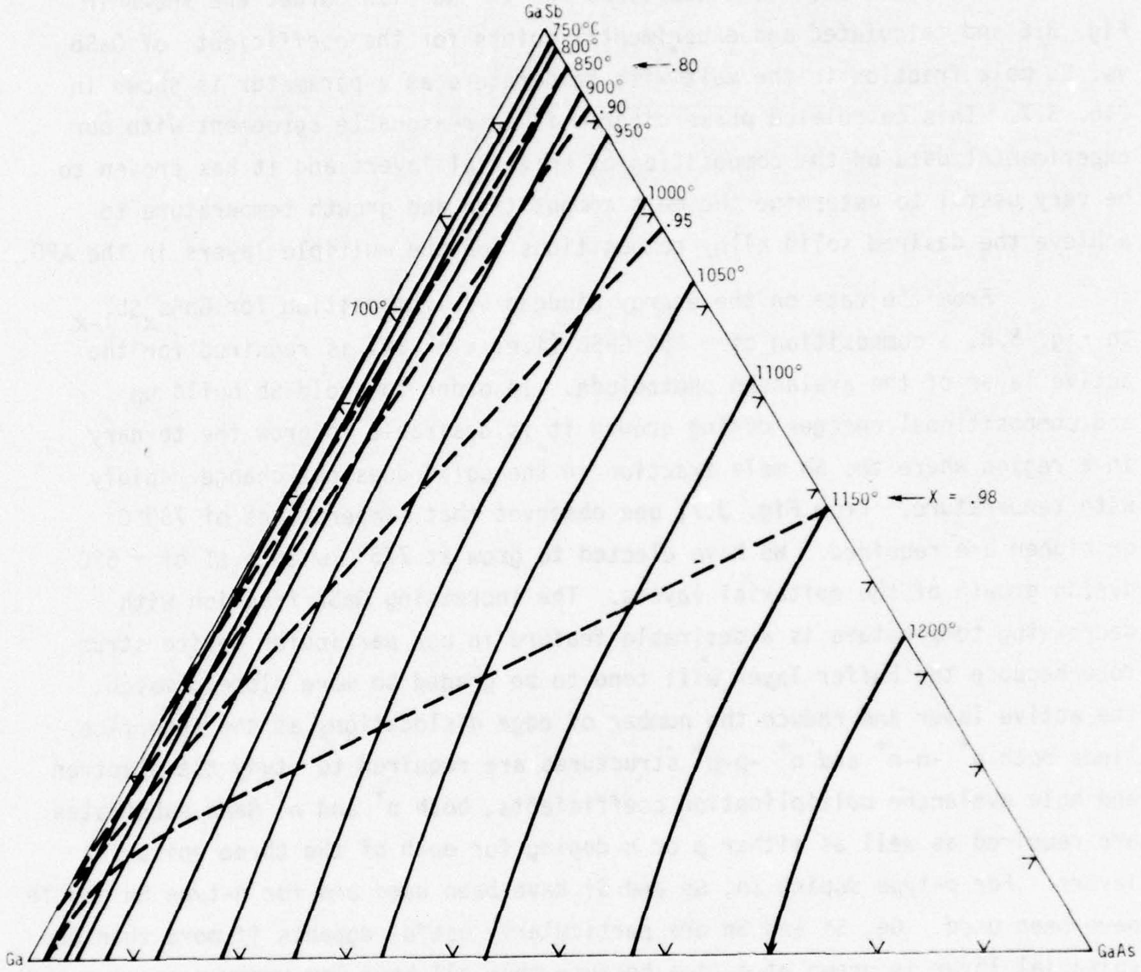

Fig. 3.6. Ga rich region of the GaAsSb phase diagram. The solid lines are liquidus isotherms while the dashed lines are $GaAs_xSb_{(1-x)}$ iso-composition lines.

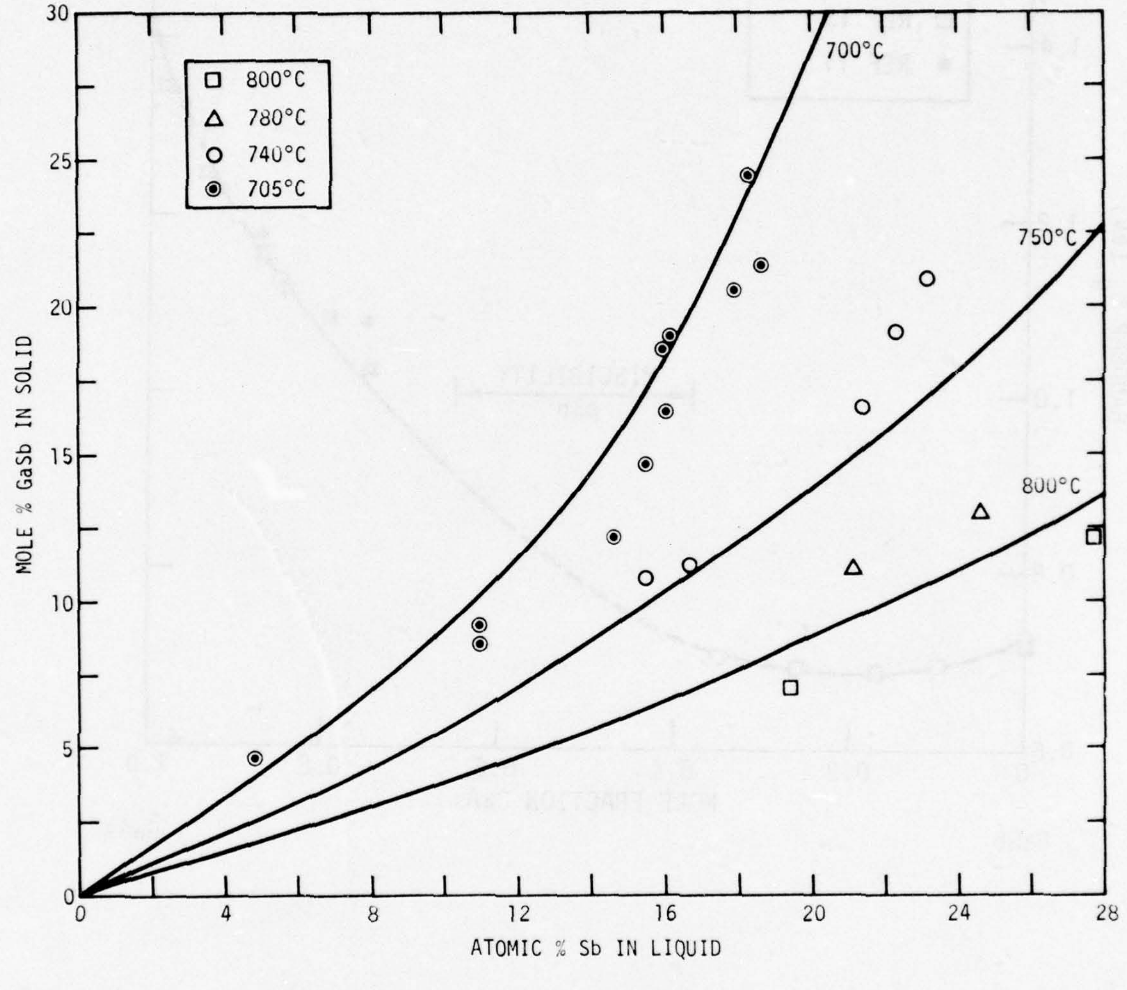

Fig. 3.7. Experimental and calculated Sb distribution curves for GaAsSb solid.

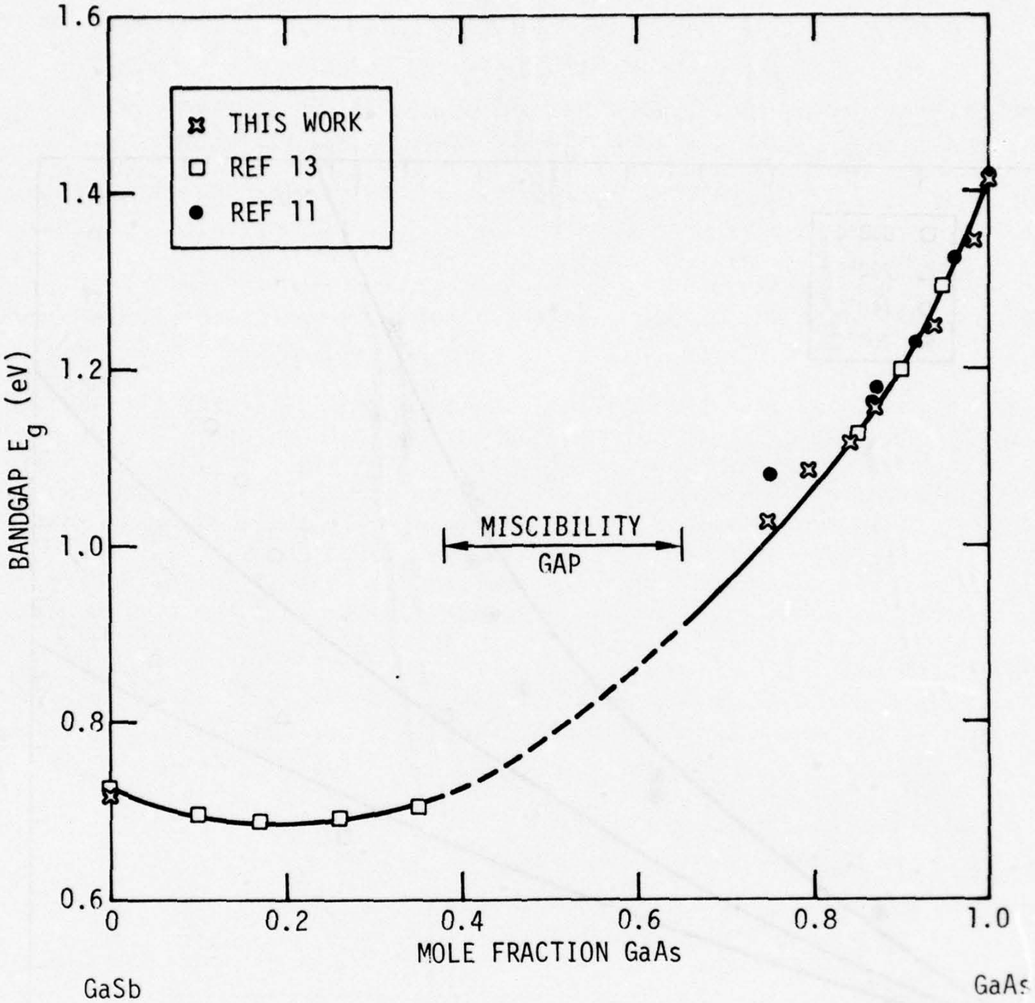

Fig. 3.8. Energy bandgap vs. composition for the $GaAs_{(1-x)}Sb_x$ alloy system. The region $0.4<x<0.65$ is inaccessible because of a miscibility gap in the alloy.

The epitaxial layer growth for any of the three layers follows the same sequence with only slight variations in the Sb concentration or the dopant to achieve the desired doping level and alloy composition. The substrates are prepared by a standard technique of mechanical lapping and polishing with successively finer grit alumina and finally a chemi-mechanical polish using Cabosil and $10H_2O:1H_2O_2$ in an oscillatory polisher. After removing the substrates from the polishing block, they are cleaned in trichloroethylene, acetone, water and methanol. The substrates are etched in $3H_2SO_4:1H_2O_2:1H_2O$ just prior to insertion into the furnace. The individual melts are made up with 6 9's Ga and 5 9's Sb from Alusuisse and Asarco respectively with between 10 and 25 atom percent Sb depending upon the desired solidus composition as shown in Fig. 3.3. Undoped polycrystal GaAs is used as the As source for saturating the melt. The substrate and melt are raised to 775°C and allowed to equilibrate for ~ 1 hour. The melt is then brought over the substrate and the furnace temperature decreased at a rate of ~ 1°C/min. After the desired temperature drop, a second melt is pulled over, then the final melt is pulled over and after the desired ΔT, the melt is pulled free from the substrate. The furnace is then cooled to room temperature and the structure is removed for evaluation.

After the structure is removed, routine evaluation consists of cleaving along a <110> plane and etching for 2-3 sec. in the A-B etch(7) to delineate the junctions. The layer thicknesses are then measured under an optical microscope. Next, "quick diodes" are fabricated by etching a mesa with a wax dot on a portion of the wafer. Tungsten probes are contacted to the diode and a photoresponse measurement is made. This measurement shows the bandgap of both the buffer and active layers and can then be used as feedback on control of the epitaxial layer compositions.

During the course of this work, considerable effort has been expended on studies of the microscopic operation of the APD. One of the most useful tools is a scanning electron microscope (SEM), particularly when combined with an energy dispersive X-ray detector and a beam induced current amplifier and monitor. This enables us to measure the chemical composition vs. depth in the epitaxial layers, the current collection efficiency and multiplication as a function of position and bias voltage and to correlate these with surface features and defects in the layers to determine if they are due to growth faults (metallic inclusions or precipitates) or substrate originated faults (dirty substrate, poor wetting or high dislocation density).

Studies of these GaAsSb heterojunction APD's and comparison with GaAs homojunction and GaAlAs-GaAs heterojunction diodes revealed that the quality of the junction is adversely affected by mismatch between the two layers. As the degree of mismatch decreased, the junctions improved. The GaAsSb diodes did not, however, show the improvement we expected when we went to a homojunction GaAsSb diode (i.e., buffer and active layer of the same composition). The problem with this structure is revealed in the X-ray profile of Fig. 3.9. This is a plot of the Sb X-ray yield vs. position for this GaAsSb homojunction structure. The interface between the two layers shows a sharp drop in Sb at the interface. This drop is coupled with a corresponding increase in the As level and is due to the condition of melt non-equilibrium when the second melt is brought over the substrate. This makes it virtually impossible to achieve the high quality junction required in the APD by the use of two melts to grow the p-n junction.

The solution to this dilemma has been to grow a true GaAsSb homojunction from a single melt by the addition of dopant during the growth. In this way, the layer composition remains constant and the impurity incorporation just changes from n-type and p-type.

This dopant drop technique imposes a slight modification of the original device design. In the initial device, the p-n junction was between the buffer and active layers. With the dopant drop technique, the p-n junction occurs midway through the active layer as shown in Fig. 3.4. This places an additional constraint on the active layer thickenss. In order to achieve the high quantum efficiency, the active layer must be nearly punched through to the buffer layer at the avalanche breakdown voltage. After several experiments with the dopant drop technique the required growth conditions were achieved.

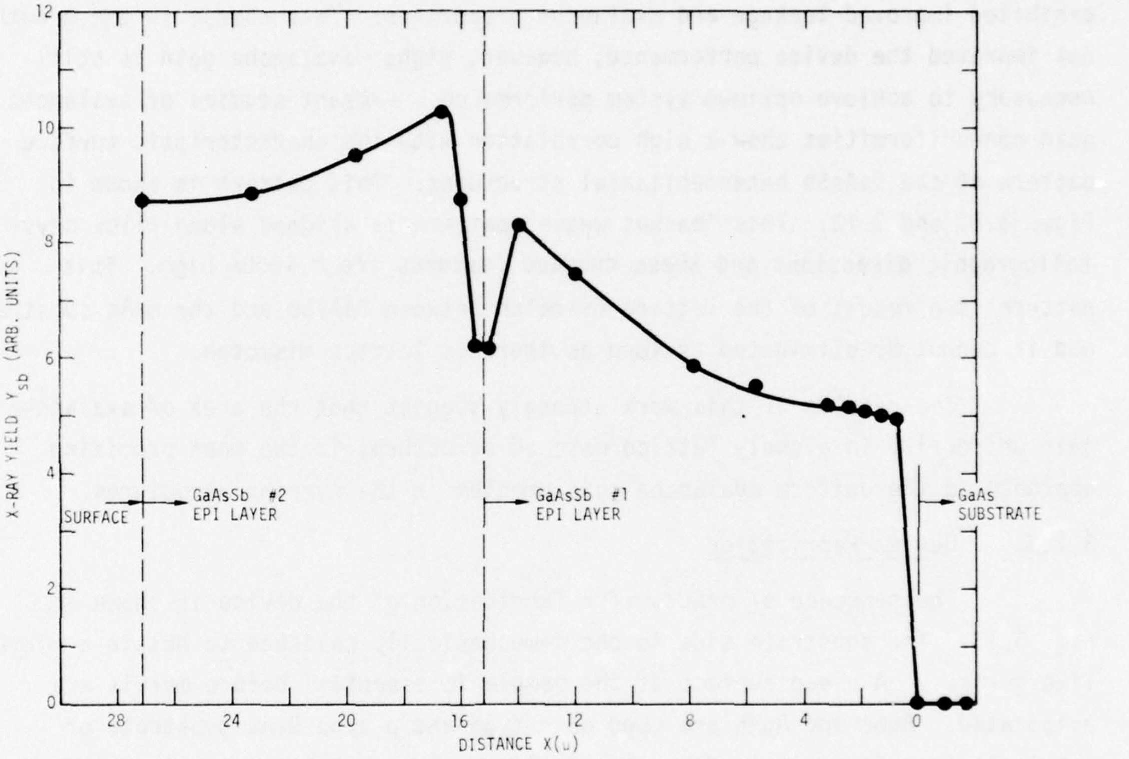

Fig. 3.9. Sb profile obtained from X-ray emission on SEM for two GaAsSb layers grown on a GaAs substrate. The melt composition for each epitaxial layer was identical but growth conditions at the time the second melt was brought over the substrate caused the Sb concentration to dip at the interface.

The dopant drop technique utilizes a boat much like our earlier versions, except a small shelf is built into the top of the slider. The slider is moved with a quartz push rod, just as earlier, except that now the rod is pulled to move the slider and pushed to move across the shelf holding the dopant. This boat and slider arrangement are shown in Fig. 3.10.

Once this doping drop technique was worked out, the resulting APD's exhibited improved leakage and avalanche properties. This change in the growth has improved the device performance; however, higher avalanche gain is still necessary to achieve optimum system performance. Present studies of avalanche gain non-uniformities show a high correlation with the characteristic surface pattern of the GaAsSb heteroepitaxial structures. This pattern is shown in Figs. 3.11 and 3.12. This "basket weave" pattern is aligned along <110> crystallographic directions and these surface features are ~ 4000Å high. This pattern is a result of the lattice mismatch between GaAsSb and the GaAs substrate and it cannot be eliminated as long as there is lattice mismatch.

The results of this work strongly suggest that the area of avalanche gain uniformity in closely lattice matched structures is the most promising approach to the uniform avalanche gain problem in the current structures.

3.2.5 Device Fabrication

The sequence of process for fabrication of the device is shown in Fig. 3.13. The substrate side is chemi-mechanically polished to obtain a mirror-like surface. A clean surface of the sample is essential before metals are evaporated. AuGe and AgMn are used on n-type and p-type GaAs substrate or GaAsSb layers respectively for metallization. The photolithographic alignment of the metallization pattern on the substrate side to the metal dots already on the layer side is made using a special mask aligner under an infrared microscope. In the transmission mode, the substrate metallization pattern and the circular dots on the layer side can be seen at the same time. After alloying the metal contacts, the ohmic contact resistance is checked. Au is electroplated over the metal contacts to protect them from pressure contacts or thermocompression bond contacts. The electroplated dots are smaller than the mesa dots

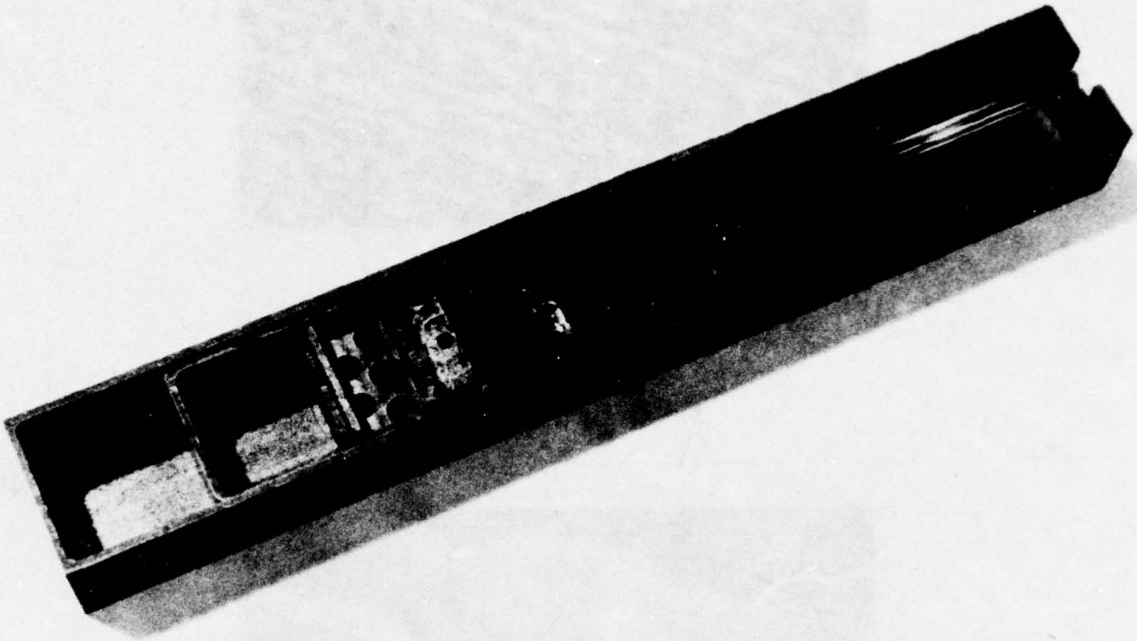

Fig. 3.10 Graphite slider boat used for "doping drop" growths. Top slider (small insert with holes) is where the dopant is placed and the quartz push rod is used to push this slider back to where the sets of holes line up and the dopant drops through into the melt to change the doping.

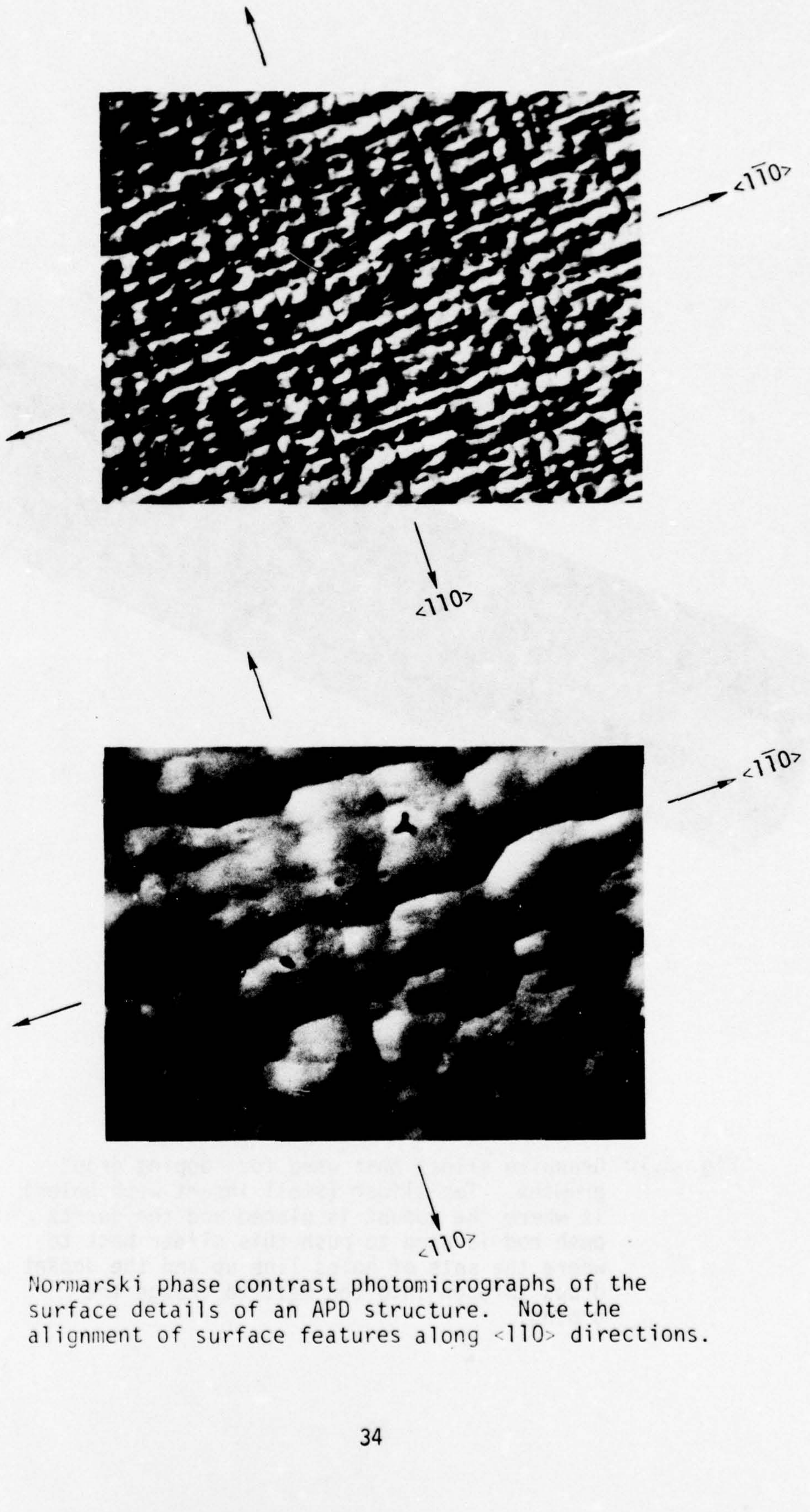
<1$\bar{1}$0>
<110>
<1$\bar{1}$0>
<110>

Fig. 3.11. Normarski phase contrast photomicrographs of the surface details of an APD structure. Note the alignment of surface features along <110> directions.

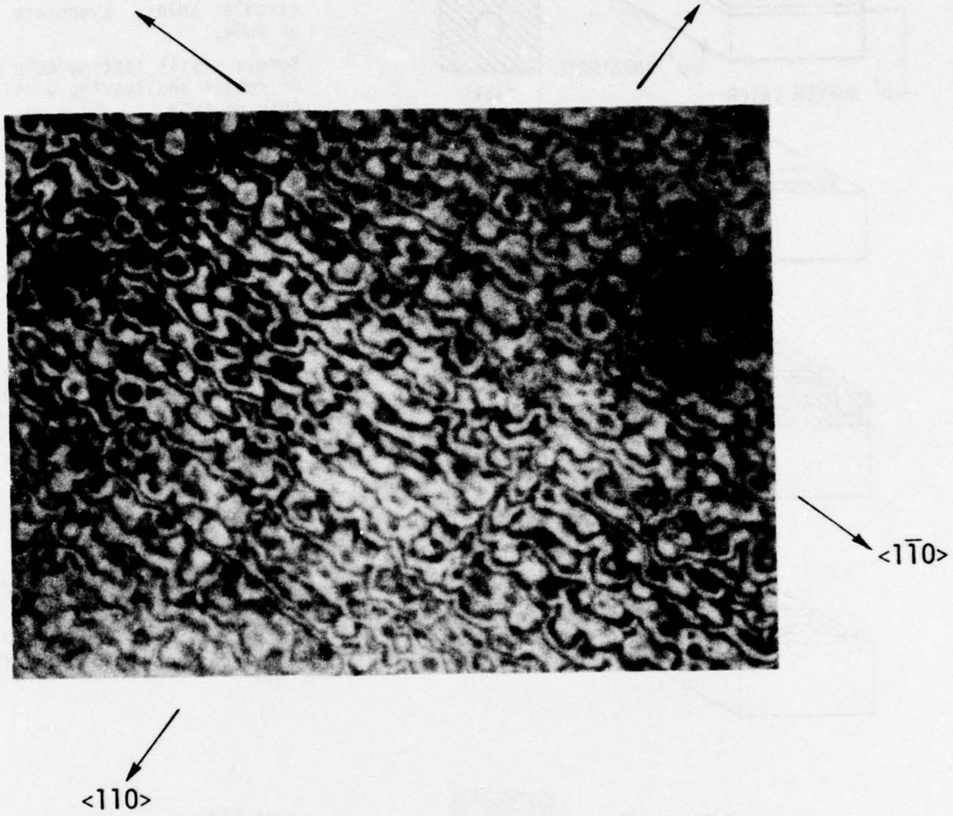

Fig. 3.12. Interference phase contrast photomicrograph of the surface of an APD structure. These surface features are between 1 and 2 fringes which corresponds to a height of 2700 to 5400Å.

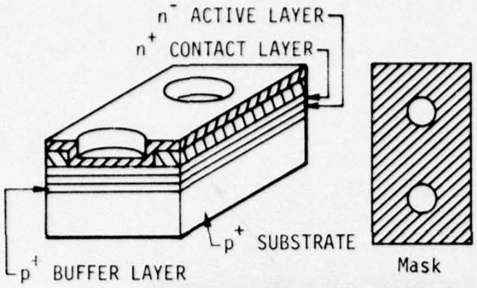

A Metallization

1) Layer Side

Apply resist and photo etch 5 mil circular holes. Evaporate 1000A of AuGe.

Remove resist lifting AuGe on top of resist and leaving 5 mil circular dots of AuGe.

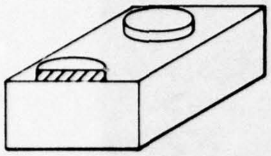

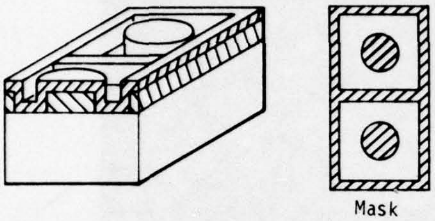

2) Substrate Side

Apply resist and photo etch 15 mil circular dots with 50 mil square outlines. Evaporate 1000Å of AgMn. Alignment of circular dots with AuGe dots on the layer side is made on an Infrared microscope.

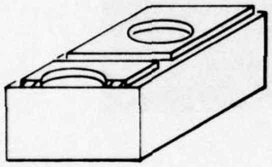

Remove resist lifting AgMn on top of resist and leaving 50 mil square of AgMn with 15 mil circular holes.

Alloy AuGe and AgMn at 500°C for 1 min.

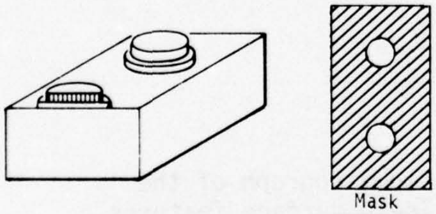

3) Layer Side

Apply resist and photo etch 4 mil circular holes over the AuGe dots. Electroplate 1 μm of Au. Remove resist leaving 4 mil circular dots of Au on top of AuGe dots.

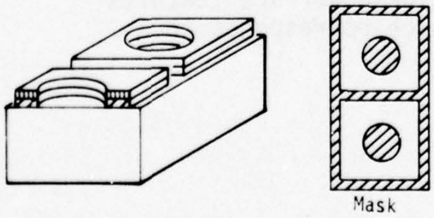

4) Substrate Side

Apply resist and photo etch 15 mil circular dots with 50 mil square outlines. Electroplate 1 μm of Au. Remove resist leaving Au on top of AgMn squares with a 15 mil circular hole.

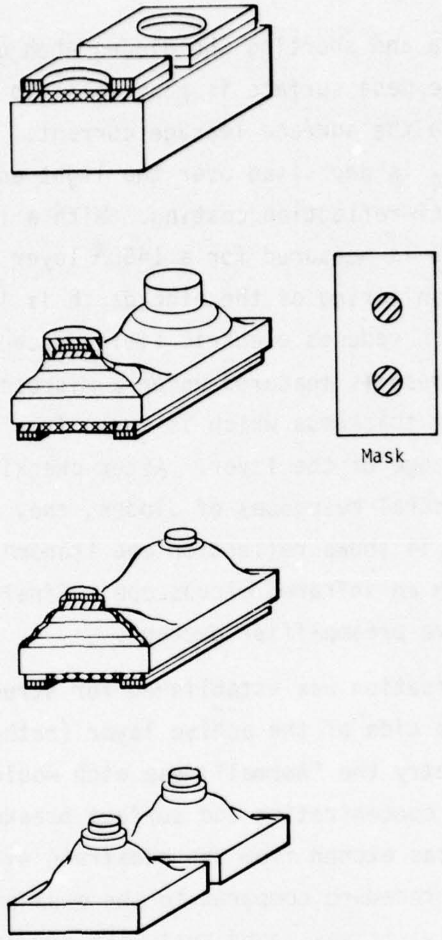

B. Anti-reflection Coating

Deposit 1450Å of Si_3N_4 by sputtering to the substrate side. Remove Si_3N_4 on top of Au by scratching the substrate side on a paper leaving Si_3N_4 inside 15 mil circular holes only.

C. Mesa Etch

1) Apply resist on the layer side and photo etch to leave 6 mil dots over Au and AuGe dots.

Etch mesa through n^+ and n layers and part of p^+ layer.

Remove resist.

D. Passivation

Apply surface passivation.

E. Device Mounting

Cleave the wafer into individual diodes. Mount the diode

Fig. 3.13 Device Fabrication Procedure for the Inverted Homo-Heterojunction Avalanche Photodiode (starting with the 3-layer epitaxial growth structure and ending with the APD chips ready for mounting or packaging).

to prevent Au from hanging over the mesa and shorting the diodes when undercutting occurs after the mesa etch. The mesa surface is passivated to protect the exposed p-n junction and to decrease the surface leakage current. To obtain maximum quantum efficiency, Si_3N_4 is deposited over the light entrance window on the substrate side for the anti-reflection coating. With a 1.06μ laser, a reflection coefficient of 0.15% is measured for a 1450Å layer of Si_3N_4 on the GaAs substrate. Careful monitoring of the etch depth is important to obtain the desired mesa geometry which reduces electric field concentration at the p-n junction. The depth of the mesa is measured under a microscope after each mesa etch and compared to the layer thickness which is known from the measurement of the cleaved and stained edge of the layer. After checking the current-voltage characteristics and spectral responses of diodes, they are cleaved into individual diodes. Fig. 3.14 shows reflection and transmission photomicrograph of a diode taken through an infrared microscope. Finally the diode is placed into the hybrid microwave preamplifier package.

Another method of device fabrication was established for structures in which the p-n junction is on the surface side of the active layer (rather than the substrate side). In this geometry the "normal" mesa etch would be expected to give surface electric field concentration and surface breakdown. The proper geometry would be to make mesas etched from the substrate side. This process is a delicate fabrication procedure compared to the mesa etching process from the layer side. Fortunately, it was found that with proper passivation techniques, mesas etched from the layer side (wrong geometry for these homo-heterostructure diodes) gave the same measurement results as the mesa etched from the substrate side (no surface breakdown). Therefore this inverted mesa fabrication method did not prove necessary and the procedures need not be described here further.

3.3 Preamp Design

In the course of this work, 3 prototype receivers were built for evaluation. The first two were built with hybrid integrated `front-ends´ and discrete subsequent stages. The third was completely hybrid integrated and is shown in Fig. 3.15.

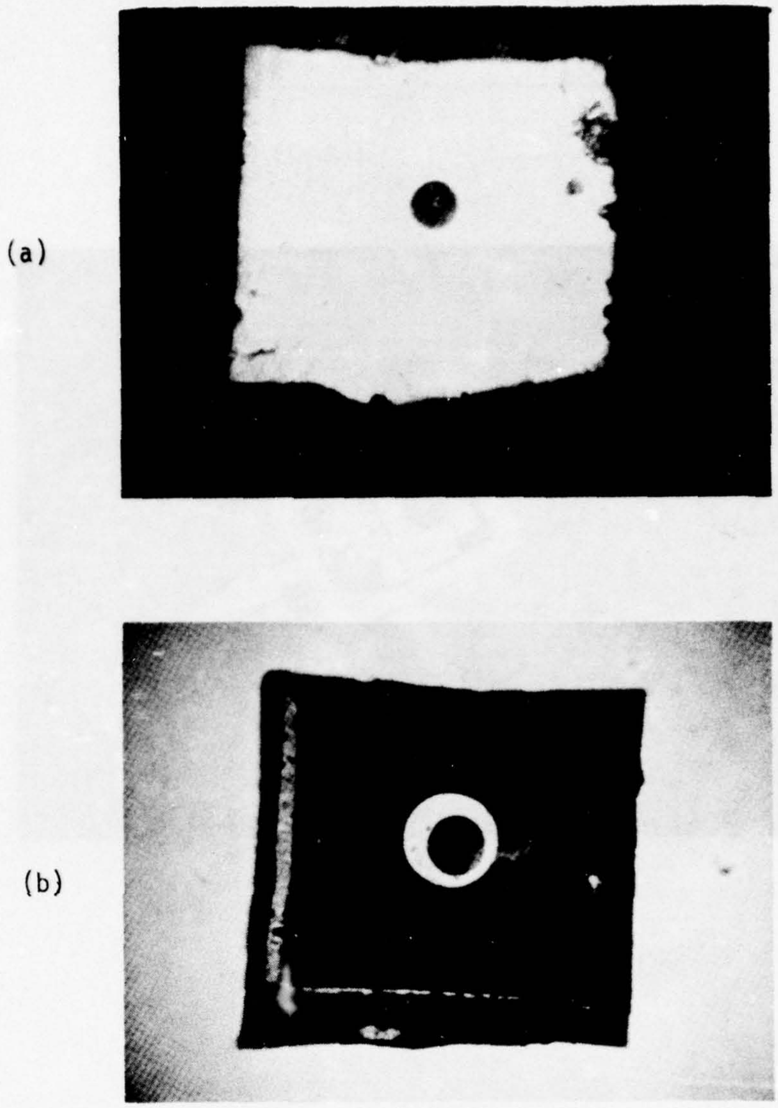

Fig. 3.14 a) Reflection photograph of a diode where the dark circular dot is the mesa outline and the metal contact in the center.

b) Transmission photograph of a diode is taken by the infrared microscope from the layer side. The dark square area is the metal contact on the substrate side. The large bright circle is the window on the substrate side. The dark circular dot is the outline of the mesa and metal contact to the contact layer.

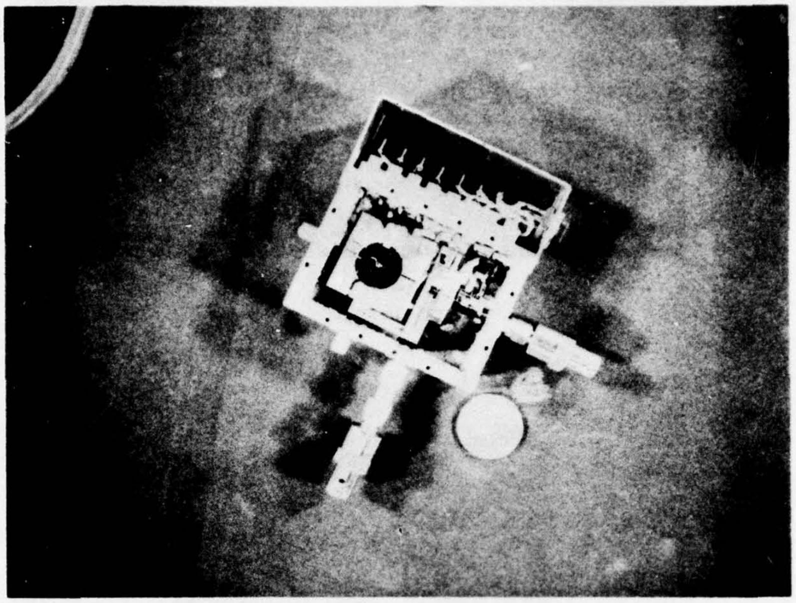

Fig. 3.15 Hybrid integrated 0-5 MHz III-V Heterojunction photodiode optical receiver

For the sake of brievity, only two circuit diagrams are shown (Figs. 3.16 and 3.17) and described. These are the circuit diagrams for receiver #1 and receiver #3. Receiver #2 was sufficiently similar to #1 that it need not be described in detail.

Referring to Fig. 3.16, we see that basically, the circuit is a Mosfet source-follower input or front-end, a cascode connected voltage amplifier consisting of Q_2 and Q_4, followed by another Mosfet source-follower. The feedback is taken from the source of this Mosfet to the summing function formed at the gate of the first Mosfet. Transistors Q_6, Q_7 provide isolation, and current gain to drive a 93Ω load. Q_1 has an input capacitance, C_{gs} of about 5 pf. In the source-follower connection, the equivalent input capacitance $C'_{gs} = C_{gs}\ (1 - A)$ where A is the voltage gain of this stage, given by $A \simeq \frac{g_M R_S}{1+g_M R_S}$ in the limit where $R_S << Z_{gs}$. So here,

$$C'_{gs} \simeq C_{gs}\left(1 - \frac{g_M\ R_S}{1+g_M R_S}\right)$$

here, the transconductance, $g_M \simeq 10\text{x}10^{-3}$ mho, $R_S = 3\text{K}$, so $C'_{gs} = 5\text{x}10^{-12}$ $(1 - .97) = 0.15$ pf. At an operating photodiode bias of about -20 VDC, the photodiode capacitance (C_{APD}) is about 0.26 pf. This gives an equivalent total input capacitance of 0.41 pf, which with R_F determines the open-loop frequency response of the complete amplifier. That is: $f_{-3dB} = \frac{1}{2\pi\ R_F\ C_i}$. The value of R_F used in this preamp was 6.12 MΩ, and the measured open-loop f_{-3dB} was 68 KHz. This implies that $C_i = 0.383$ pf, very close to the 0.41 pf predicted value. This shows that the stray capacitance has been successfully minimized.

As will be recalled from Section 2, the gain bandwidth product desired for the voltage gain section is greater than 3 GHz. So we need high open-loop gain and wide bandwidth. The required voltage gain can be achieved with a common-emitter stage. However, in such an arrangement, the Miller effect capacitance severely limites bandwidth. For this reason a cascode configuration

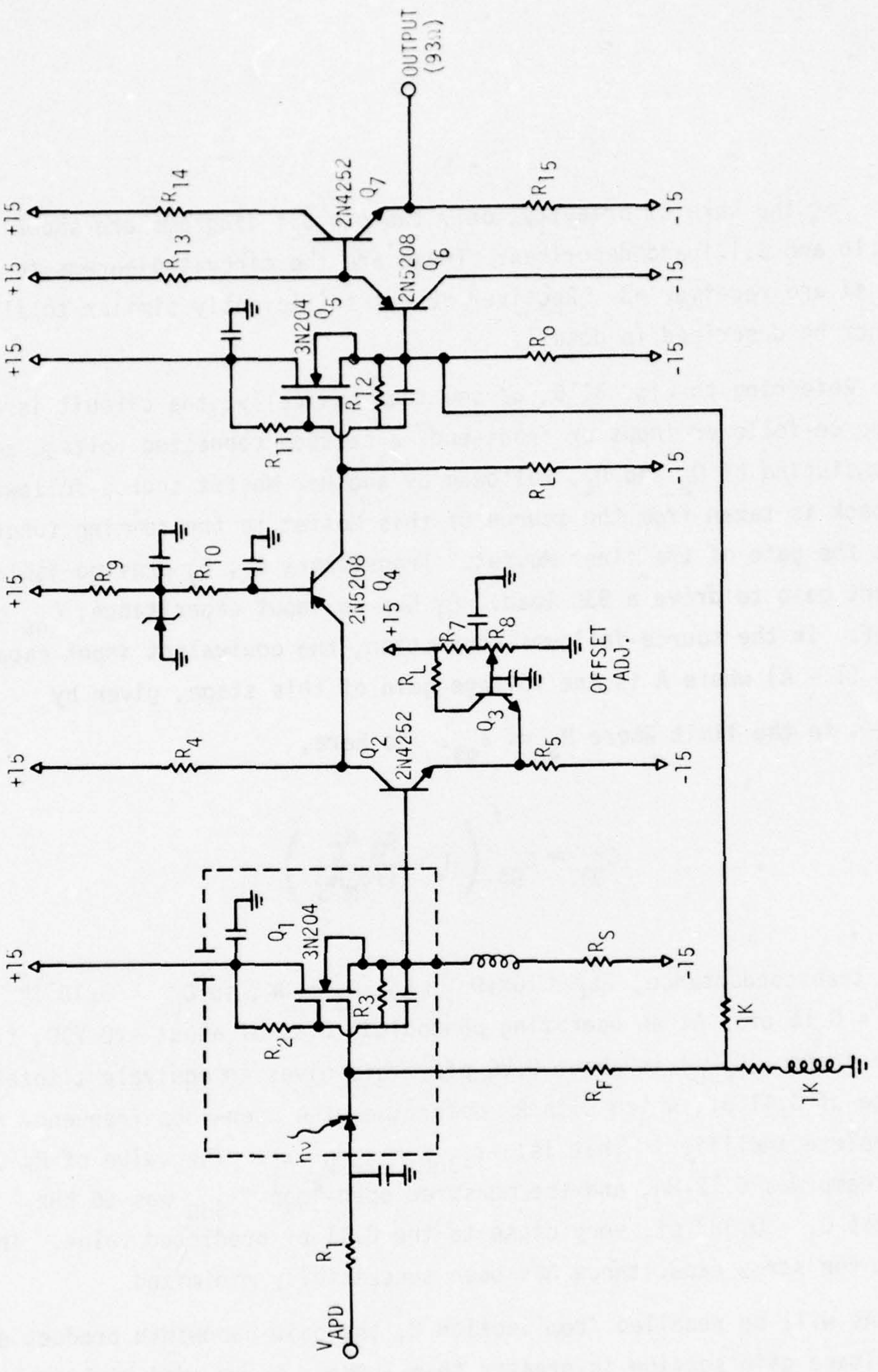
OUTPUT
(93Ω)
2N4252
Q_7
R_{14}
R_{13}
R_{15}
2N5208
Q_6
3N204
Q_5
R_{12}
R_{11}
R_0
R_L
R_9
R_{10}
2N5208
Q_4
R_7
R_8
OFFSET ADJ.
R_L
Q_3
R_5
R_4
Q_2
2N4252
Q_1
3N204
R_2
R_3
R_S
1K
R_F
1K
hν
R_1
V_{APD}
+15
-15

Fig. 3.16 SCHEMATIC DIAGRAM RECEIVER #1

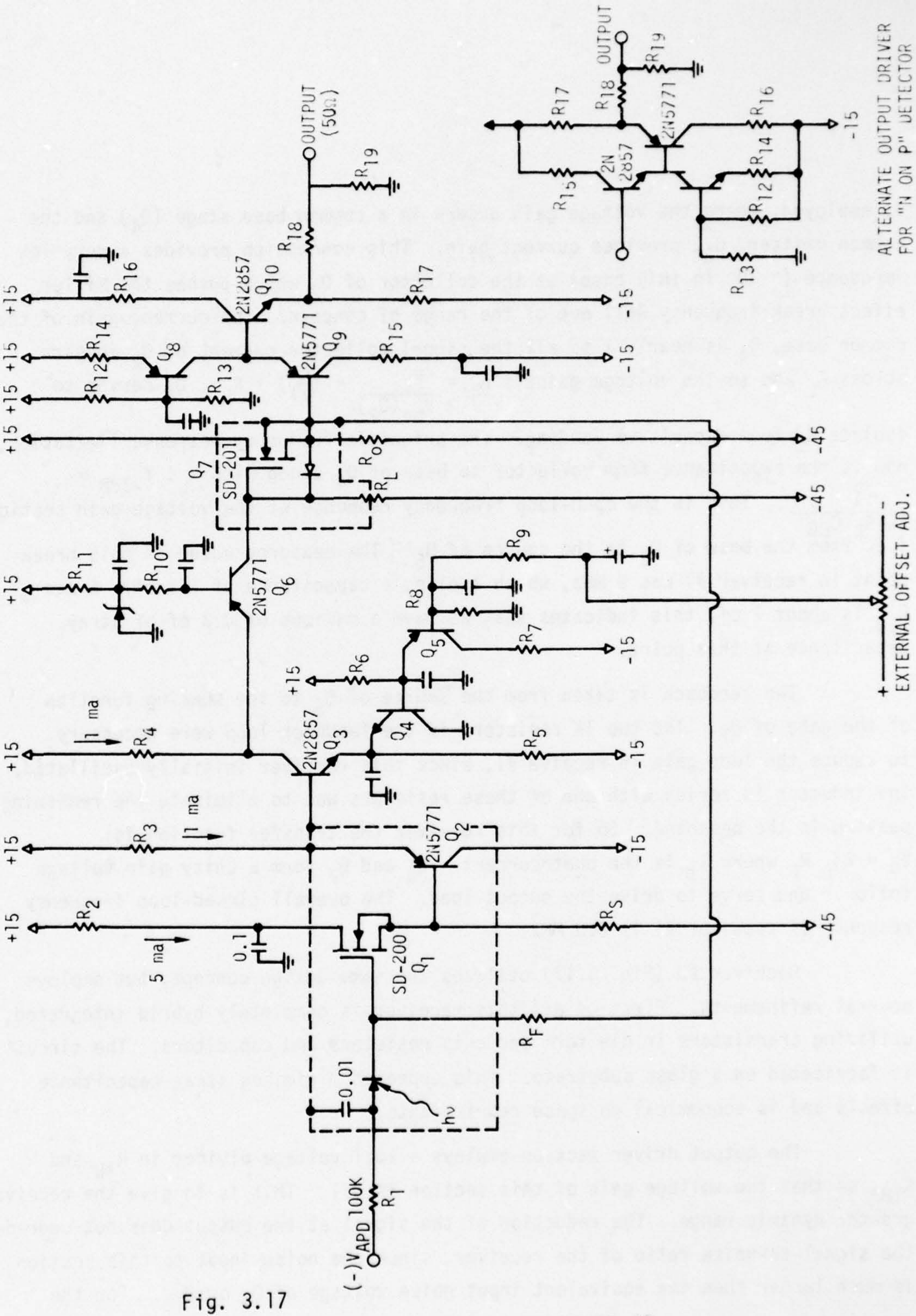

+15
R2
5 ma
0.1
SD-200
Q1
RF
0.01
hν
R1
100K
(-)VAPD
+15
R3
1 ma
2N5771
Q2
-15
RS
-45
+15
1 ma
R4
2N2857
Q3
Q4
R5
-15
+15
R6
Q5
R7
-15
R8
R9
+15
R11
R10
2N5771
Q6
SD-201
Q7
R0
RL
-45
-45
+
-
EXTERNAL OFFSET ADJ.
+15
+15
+15
+15
R12
R13
Q8
R14
2N5771
Q9
R15
-15
2N2857
Q10
R16
R17
R18
R19
OUTPUT (50Ω)
R13
R12
R15
2N 2857
2N5771
R14
R16
-15
R17
R18
R19
OUTPUT
ALTERNATE OUTPUT DRIVER FOR "N ON P" DETECTOR

Fig. 3.17

SCHEMATIC DIAGRAM RECEIVER #3

is employed, where the voltage gain occurs in a common base stage (Q_4) and the common emitter, Q_2, provides current gain. This connection provides a very low impedance ($\sim 30\Omega$ in this case) at the collector of Q_2 which pushes the Miller effect break frequency well out of the range of concern. The current gain of the common base, Q_4 is nearly 1 so all the signal collector current of Q_2 appears across R_L and so the voltage gain is $A_V = \frac{V_{R_L}}{V_{be}(Q_2)} = (\frac{q}{kT})\, i_c R_L$. Q_5 serves to isolate R_L from capacitive loading. The principle frequency response limitation, now is the capacitance from collector to base of Q_4 along with R_L: $f_{-3dB} = \frac{1}{2\pi R_L C_{CB}}$. This is the open-loop frequency response of the voltage gain section, i.e. from the base of Q_2 to the source of Q_5. The measured value of this breakpoint in receiver #1 was 9 MHz, which implies a capacitance of 1.3 pf. Since C_{CB} is about 1 pf, this indicates that we have a maximum of 0.3 pf of stray capacitance at this point.

The feedback is taken from the source of Q_5 to the summing function of the gate of Q_1. The two 1K resistors in the feedback loop were necessary to reduce the loop gain in receive #1, since this receiver initially oscillated. The inductor in series with one of these resistors was to eliminate the remaining peaking in the passband. So for this receiver the transfer function is: $V_O = 2 i_p R_F$ where i_p is the photocurrent. Q_6 and Q_7 form a unity gain voltage follower and serve to drive the output load. The overall closed-loop frequency response of receiver #1 is 6.9 MHz.

Receiver #3 (Fig. 3.17) utilizes the same design concept, but employs several refinements. First of all this receiver is completely hybrid integrated, utilizing transistors in die form and chip resistors and capacitors. The circuit is fabricated on a glass substrate. This approach minimizes stray capacitance effects and is economical on space requirements.

The output driver section employs a 10:1 voltage divider in R_{19} and R_{18}, so that the voltage gain of this section is 0.1. This is to give the receiver greater dynamic range. The reduction of the signal at the output does not degrade the signal-to-noise ratio of the receiver, since the noise input to this section is much larger than the equivalent input noise voltage of Q_9 or Q_{10}. For the output Mosfet, a Signetics SD-201 is used. This device has very low equivalent input capacitance (C_{gs} = 2 pf vs. C_{gs} = 5 pf in the 3N204 devices used in receiver #1) and has a protective diode between its gate and source. Such a diode, of course, could not be used in the first stage Mosfet, since it would intollerably increase the shot noise at the input due to its leakage current. The only other differences are the use of SD-200 Mosfet at the input rather than the 3N204, use of an additional emitter follower, Q_2, and a -45 VDC power supply terminating R_S, R_L, R_0. The SD-200 has a gate to source capacitance a factor of 2 lower than the 3N204, however, it has nearly 4 times more equivalent input spectral noise voltage density ($\sim$ 22 nV/$\sqrt{Hz}$). This was deemed a reasonable tradeoff since the noise voltage as a function of frequency is proportional to $e_n C\omega$, where e_n is the noise voltage density, C is the input capacitance and ω is the circular frequency. This relationship will be explained in more detail later.

The desirability of the other refinements can best be understood by considering the model for the Mosfet in the source-follower configuration. Fig. 3.18 shows that both the voltage gain of this stage and the input conductance depend on the load conductance. It is, therefore, desirable to make the load conductance as small as possible, e.g. make the load impedance as large as possible, while maintaining the same quiescent drain current. To do this, the -45V power supply was used on both Mosfets. Also to reduce the capacitive part of Z_L (the load impedance), the additional emitter follower, Q_2 was added. So that now the input Mosfet need only drive the load R_S and the capacitance of this emitter follower and does not have to drive the input guard (the dotted line in Fig. 3.17).

3.4 Design & Fabrication of Feedback Resistance Element

As mentioned before, one of the key factors affecting the realization of the receivers discussed here is the feedback resistance element. This resistor is required to have a feed-through capacitance (C_F) of $\lesssim 10^{-15}$ F and the distributed stray capacitance from this resistor to ground (C_{SH}) is to be $\leq 10^{-15}$F. The former requirement stems from the limitation C_F places on

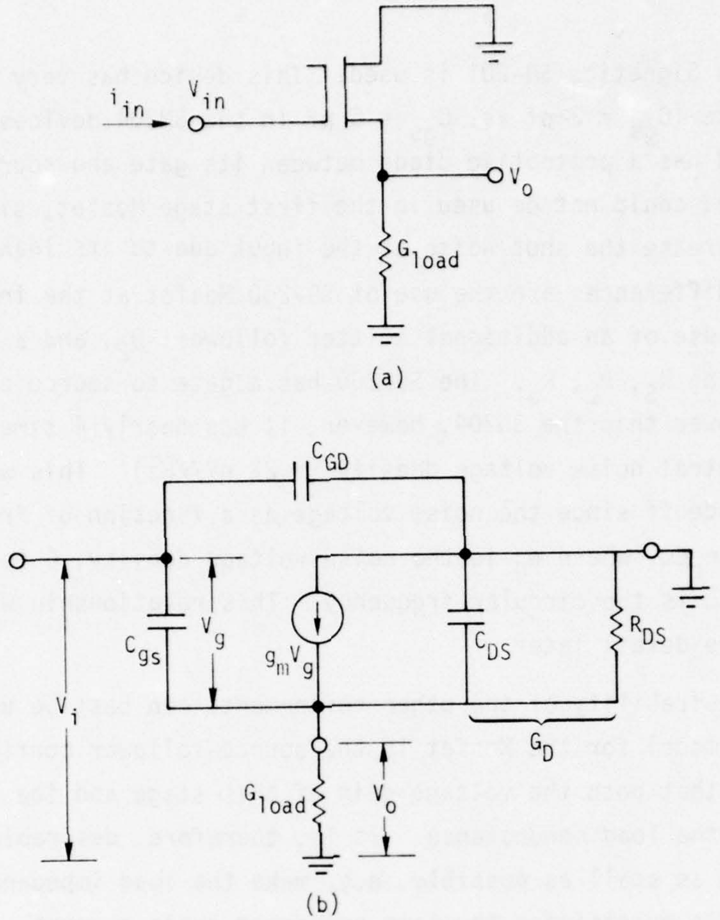

i_{in}
V_{in}
V_o
G_{load}
(a)
C_{GD}
C_{gs}
V_g
$g_m V_g$
C_{DS}
R_{DS}
V_i
G_D
G_{load}
V_o
(b)

VOLTAGE GAIN: $\frac{V_o}{V_i} = \frac{g_m + G_g}{g_m + G_D + G_L + G_g}$

INPUT CONDUCTANCE: $G_i = \frac{i_{in}}{V_{in}} = G_F + \frac{G_g\ (G_D + G_L)}{g_m + G_D + G_L + G_g}$

WHERE: g_m is the device transconductance and

$G_g = jwC_{gs}$, $G_D = jwC_{DS} + 1/R_{DS}$, $G_L = jwC_{load} + 1/R_{load}$

Fig. 3.18 Signal model for single gate Mosfet in source follower configuration

bandwidth, and the latter from the phase shift which C_{SH} introduces.

A design satisfying these requirements and the final result of our efforts at obtaining such a component is illustrated in Fig. 3.19. The actual resistance element is the thin line in the middle. It is 10μ wide by 2 mm long. The broader lines, terminated at the squares at each end are aluminum contacts. The device is altogether 6 mm long (≃ .24") and is deposited on a 7059 type glass substrate. The resistance material is cermet which is composed of chromium (Cr) and silicon-monixide (SiO). Depending on the ratio of Cr to SiO used in the composition of the resistor, an extemely wide range of resistivities is obtainable.(5) This is an advantage of our evaporation system and will permit us on subsequent receivers to evaporate all the circuit resistors directly on the circuit substrate.

The apparatus, shown in Fig. 3.20, consists of a sample chamber (upper part) where the substrate is loaded and held, face down, near the top of the chamber. It is heated to the desired temperature by radiation from a naked tungsten filament. Near the bottom of this chamber are 2 crucibles containing the SiO and Cr. These crucibles are each heated by separately controlled electron beams. The openings on these crucibles are baffled such that when the sources reach the proper temperature, the evaporant stream forms a cone from each crucible and the bases of these cones overlap at the sample. The sample is initially shuttered and the rate of evaporation from each source is monitored (with Sloan crystal thickness monitors) until the rate of each evaporant when corrected for its density will result in the desired ratio of Cr to SiO. Once this condition has been established, the shutter in front of the sample substrate is opened while the changing resistivity is being continually monitored. When the desired resistivity has been reached, the shutter is closed and the evaporation is complete.

The sample chamber is pumped from atmosphere by two vac-sorb pumps to a pressure of about 1 micron. Then it is pumped to a standby pressure of 10^{-9} torr by a Granville-Phillips Electro-ion pump. During evaporation, this same pump is in operation and a pressure of about 10^{-6} torr is maintained.

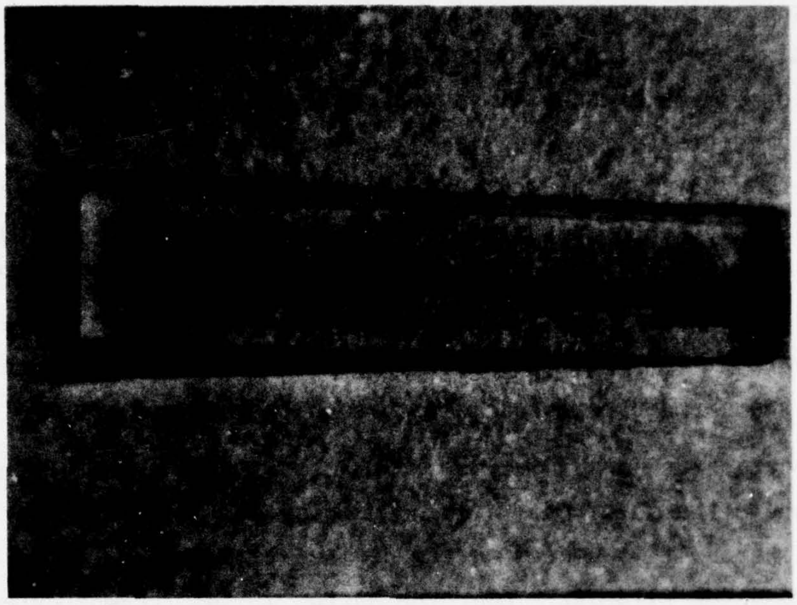

Fig. 3.19 Low capacitance cermet resistance element

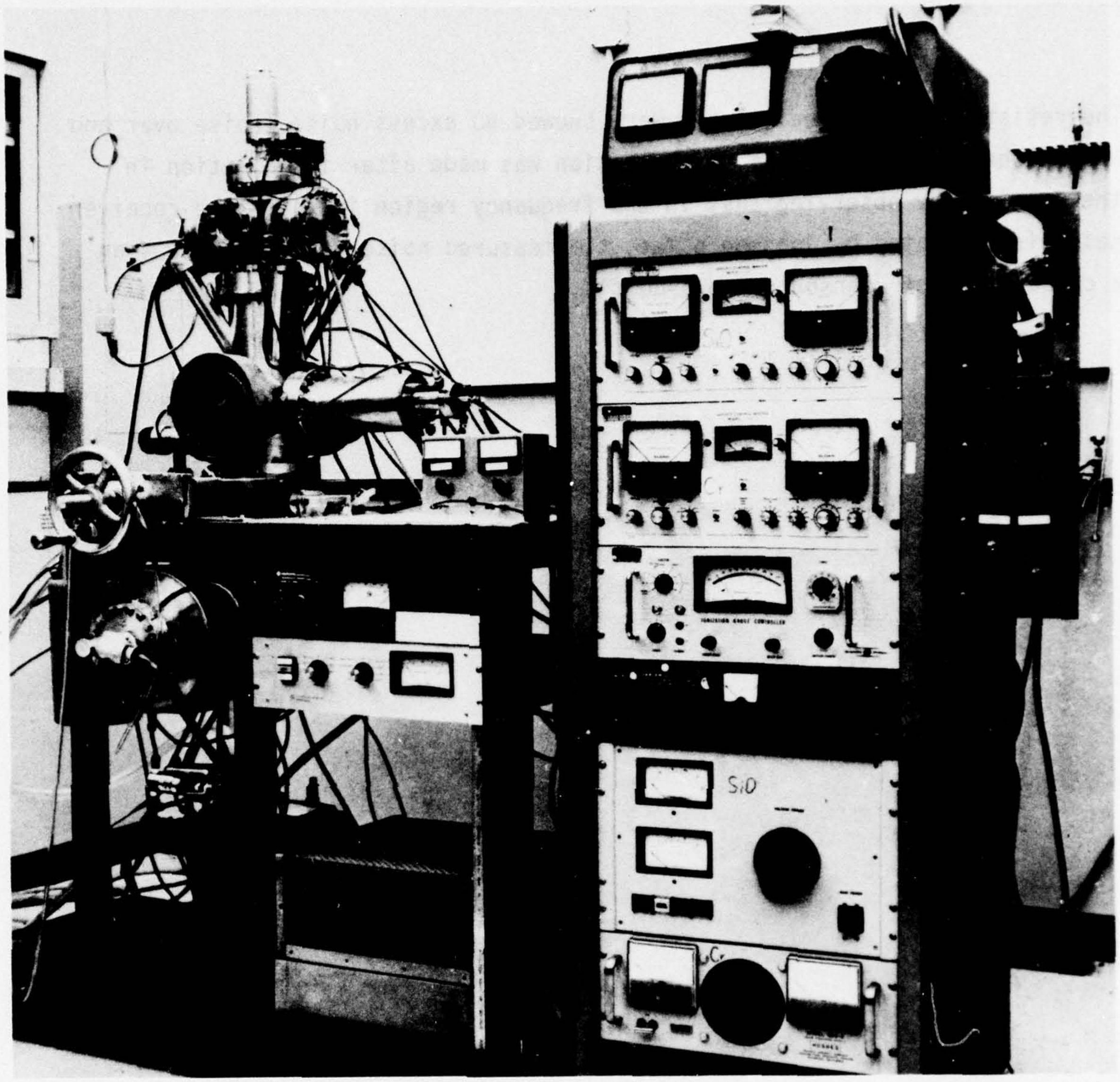
SiO
Cr
SiO
Cr

Fig. 3.20 Cermet resistor evaporation apparatus

The resistors fabricated in this way, showed no excess noise (noise over and above Johnson noise). This determination was made after installation in the receiver by observing that in the frequency region in which the receiver noise is dominated by Johnson noise, the measured noise was no higher than a calculation of Johnson noise predicts.

4.0 MEASUREMENT TECHNIQUES

The principal measurement systems employed for the evaluation of these receivers were the Tektronix Digital Processing Oscilloscope (DPO) system, and the Tektronix Model 7L13 Spectrum Analyzer (~ 1 KHz to 1.8 GHz). In addition, the HP Model 313A Tracking Oscillator and 312B selective voltmeter combination was used as well as the HP Model 3400-A true RMS voltmeter.

4.1 Open-Loop Frequency Response

The first important parameter to be measured on the receiver is the open-loop gain-phase vs. frequency. The receiver configuration for this measurement is indicated in Fig. 4.1. Here the feedback loop is broken and a signal is injected into the feedback resistor as shown. The magnitude and phase of the output signal is then compared with this input to determine gain and phase-shift. This measurement is relatively easy in the passband of the amplifier where the output signal is large, and can be accomplished with a Vector voltmeter. In fact, the -3dB point determined by $f_{-3dB} = \frac{A}{2\pi R_F C_i}$ (where C_i is the total equivalent input capacitance of the receiver, including C_{APD}) can be measured this way and C_i thus determined. However, important information regarding the phase-margin and hence stability is contained in the response at frequencies much higher than the f_{-3dB} point. At these frequencies the output is small in magnitude and sometimes almost totally buried in noise; so that the direct measurement of gain and phase is impractical. One of the functions contained in the DPO software is the correlate function. The cross-correlation of an equal number of cycles of two sine-wave functions of equal frequency is illustrated in Fig. 4.2(b). From the magnitude and location of the peak of this function, both the ratio and phase of these sine-waves can be determined. Since the computation for each point of the cross-correlation utilizes the whole input waveform, a considerable increase in signal-to-noise ratio is achieved. This point is illustrated in Fig. 4.2. Fig. 4.2(a) shows the two sine-waves used in obtaining the cross-correlation function shown in Fig. 4.2(b). Note that one sine-wave is unrecognizable.

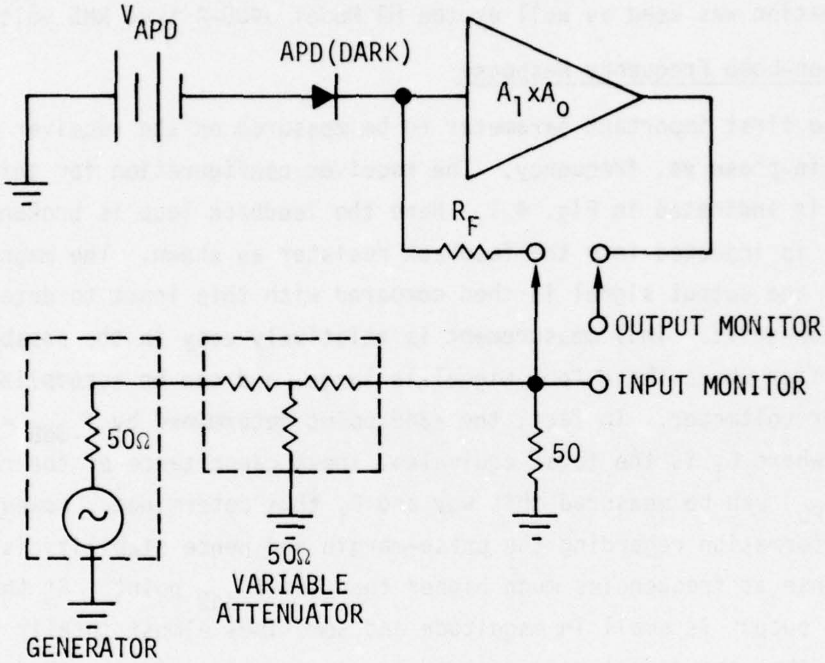
V_{APD}
APD(DARK)
$A_1 x A_o$
R_F
OUTPUT MONITOR
INPUT MONITOR
50Ω
50
50Ω
VARIABLE
ATTENUATOR
GENERATOR

Fig. 4.1. Experimental configuration for measurement of open loop gain-phase.

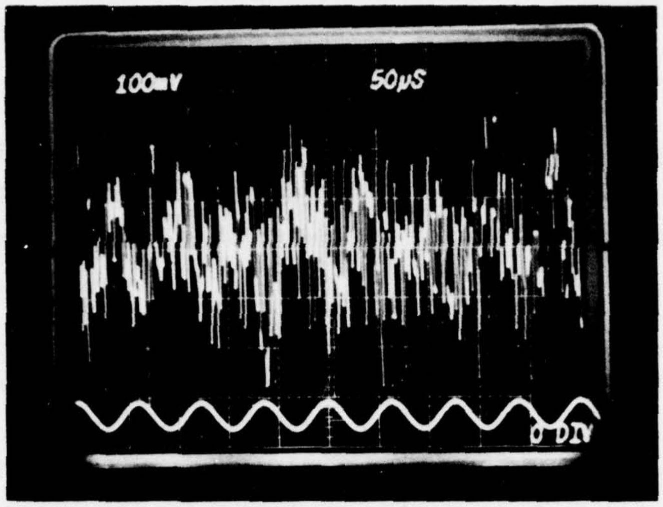

(a)

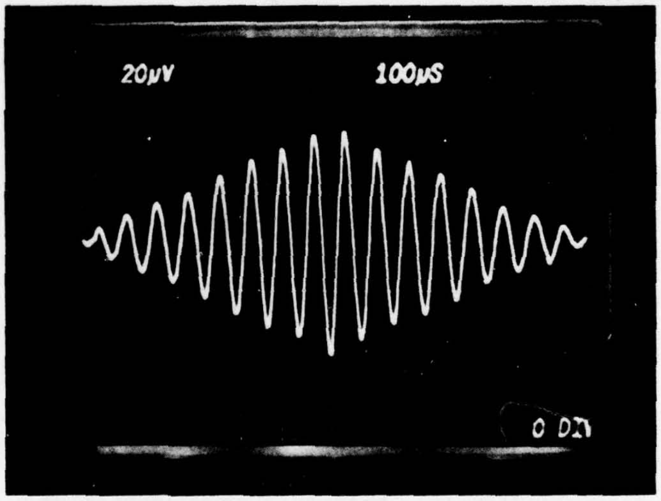

(b)

Fig. 4.2. (a) 8 cycles of two sine waves of equal frequency. One sine wave totally buried in noise.

(b) Cross-correlation of the two sine waves in (a).

By utilizing this function in a program written to run on the DPO, measurements of open-loop gain-phase were performed at frequencies in excess of 10 MHz and the behavior of the phase near the point at which the gain approaches zero was observed.

4.2 Closed-Loop Frequency Response

The closed-loop frequency response of the receiver could be measured directly if a 1.06μm light source which could be sine-wave modulated up to 10 MHz were available. Since such a light source is not available at our laboratory, we had to devise another technique for this measurement.

A special top cover for each receiver was fabricated in which a shielded cable was supported with its central conductor about 0.1" from the summing junction of the amplifier (see Fig. 4.3). Thus a small capacitance (C_c) was formed. The value of this capacitor was determined by injecting a triangular waveform and observing the output square wave. The value of C_c is then obtained as indicated in Fig. 4.3. This value was of the order of 10^{-15}F for all three receivers constructed.

Once the C_c is installed and calibrated then the response of the amplifier to a voltage step of known height (Fig. 4.3(a)) is the impulse response of the amplifier. Applying another function in the DPO software, the Fast Fourier Transform (FFT), to a digitally stored replica of this impulse response gives the frequency response, from which the closed-loop f_{-3dB} can be determined. For all of the measurements where a repetitive waveform is to be digitally stored in the computer, another very useful feature of the DPO system software is signal averaging. In this way the signal-to-noise ratio of various responses can be improved significantly before further processing.

4.3 Noise Measurements

Measurement of total noise in a given bandwidth can be done directly by a true RMS voltmeter. This, however, gives no information about the statistical distribution of the noise. That is to say we do not know with what frequency a given instantaneous voltage value above or below the mean occurs. Whether this distribution is Gaussian or not determines the presence or absence

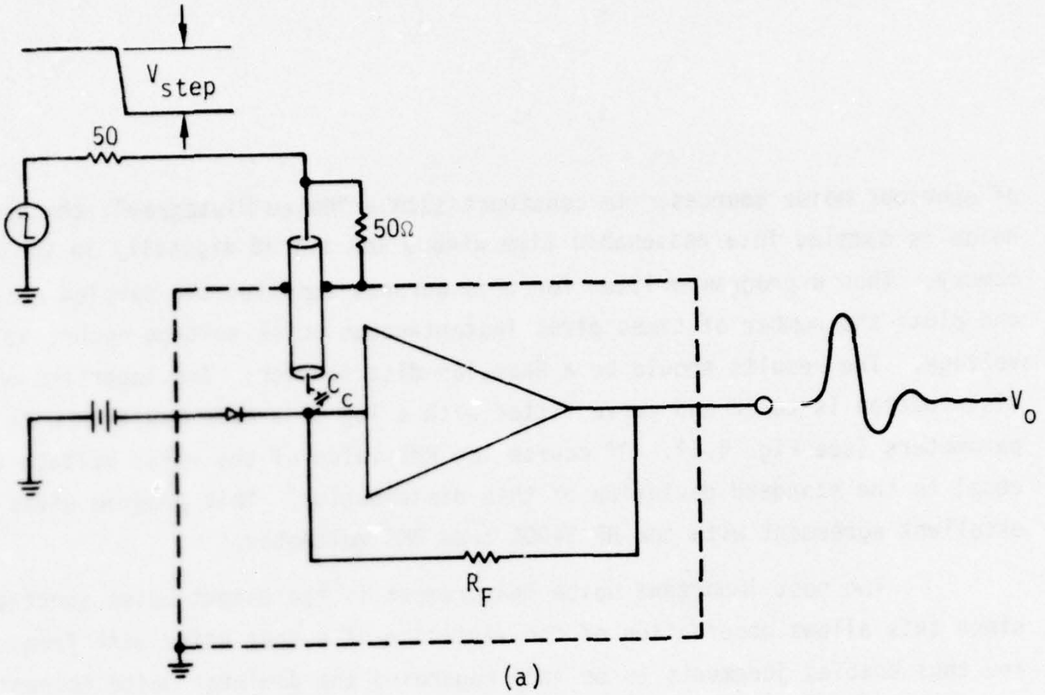
V step
50
50Ω
C c
V o
R F

(a)

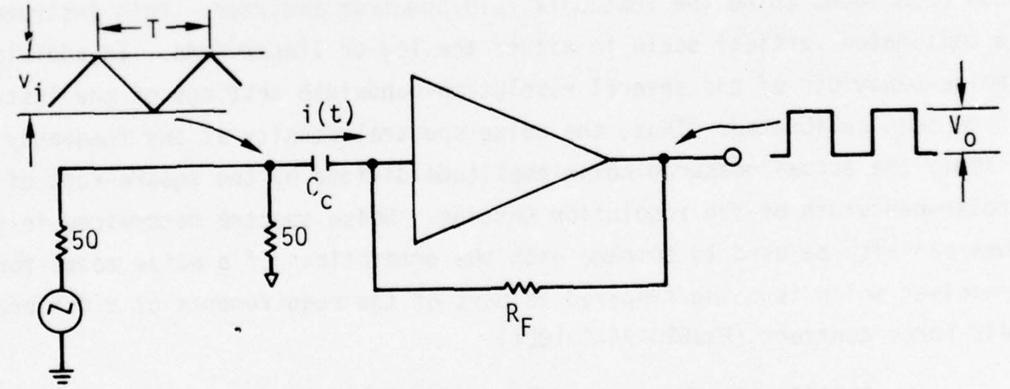
T
v i
i(t)
C c
50
50
R F
V o

$$v_i = \frac{dv_i}{dt} \times t = \frac{dv_i}{dt}\,(T/2) \Longrightarrow \frac{dv_i}{dt} = \frac{2v_i}{T}$$

$$v_o = R_o\, i(t)\ ;\ i(t) = C_c\,\frac{dv_i}{dt} \Longrightarrow v_o = R_o C_c\,\frac{dv_i}{dt}$$

$$\boxed{C_c = \frac{v_o}{R_o\,\left(\frac{dv_i}{dt}\right)}}$$

(b)

of spurious noise sources. To construct such a "Noise Histogram", the output noise is sampled in a reasonable time window and stored digitally in the DPO memory. Then a program written for this purpose compiles the sampled noise and plots the number of times given instantaneous noise voltage occurs vs. that voltage. The results should be a Gaussian distribution. The logarithm of this distribution is taken and curve fitted with a log of a true Gaussian with the same parameters (see Fig. 4.4). Of course the RMS value of the noise voltage is equal to the standard deviation of this distribution. This program gives excellent agreement with the HP 3400A true RMS voltmeter.

The most important noise measurement is the output noise spectrum, since this allows observation of the variation of output noise with frequency and thus enables judgments to be made regarding the dominant noise mechanisms in different frequency ranges. The most convenient way to make this measurement has been found to be the Tektronix 7L13 spectrum analyzer. This instrument has a calibrated vertical scale in either the log or linear mode. In addition, the noise-bandwidth of the several resolution-bandwidth settings of the instrument have been calibrated. Thus, the noise spectral density at any frequency is simply the actual measured noise amplitude divided by the square-root of the noise-bandwidth of the resolution setting. Noise spectra determined in this way can also be used to compare with the predictions of a noise model for the receiver which is being prepared as part of the requirements of a different Air Force contract (F33615-76-C-1001).

Another important measurement possible with the 7L13 is the direct measurement of noise equivalent current (NEI) from which noise equivalent power (NEP) can be computed. By definition, noise equivalent power is that power at which the signal is just equal to the noise. In general:

$$V_{sig+noise}^{2} = (V_{sig})^2 + (V_{noise})^2 \quad . \text{ If } V_{sig} = V_{noise},$$

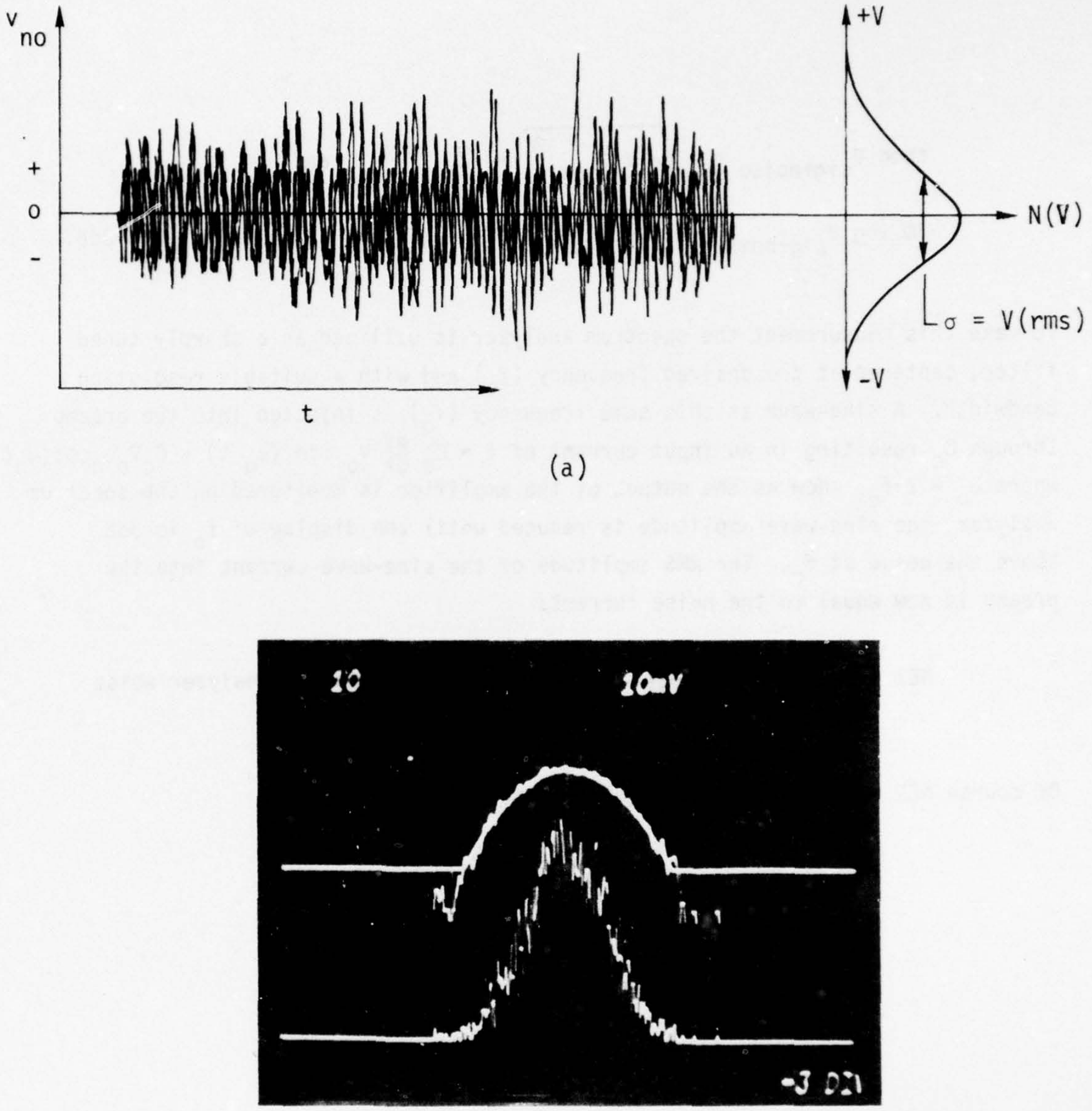

(a)

Fig. 4.4 (a) Noise output and its statistical distribution.

(b) Measured statistical distribution of output noise, its log superimposed with log of a Gaussian distribution.

$$\text{then } V_{\text{sig+noise}} = \sqrt{2(V_{\text{noise}})^2} = \sqrt{2}\ V_{\text{noise}} \text{ and:}$$

$$20 \log V_{\text{sig+noise}} = 20 \log V_{\text{noise}} + 20 \log \sqrt{2} \qquad V_{s+n}(\text{dB}) = V_n(\text{dB}) + 3\text{dB}.$$

To make this measurement the spectrum analyzer is utilized as a sharply tuned filter, centered at the desired frequency (f_o) and with a suitable resolution bandwidth. A sine-wave at this same frequency (f_o) is injected into the preamp through C_c resulting in an input current of $i = C_c \frac{dv}{dt} V_o \text{ Sin } (\omega_o t) = C_c V_o \omega_o \cos(\omega_o t)$ where $\omega_o = 2\pi f_o$. Now as the output of the amplifier is monitored on the spectrum analyzer, the sine-wave amplitude is reduced until the display of f_o is 3dB above the noise at f_o. The RMS amplitude of the sine-wave current into the preamp is now equal to the noise current:

$$\text{NEI} = \frac{C_c\ V_{3dB}(\text{RMS})\ \omega_o}{\sqrt{\Delta F}}$$, where ΔF is the spectrum analyzer noise bandwidth.

Of course $\text{NEP} = \frac{h\nu}{\eta}$ (NEI) = 1.226 (NEI) in our case.

5.0 RESULTS OF MEASUREMENTS

5.1 Measurement and Analysis of Signal Response

Table 3 shows some of the actual measured parameters of the three prototypes that were fabricated.

Fig. 5.1(a) shows the actual frequency response for receiver #3 determined by operating on the impulse response with the Fast Fourier Transform (FFT) on the DPO, and Fig. 5.1(b) shows this corrected to a dB scale and plotted against the log of frequency. The value at low frequency corresponds to $\frac{V_o}{i_p} = R_o \simeq 12.4 \times 10^6$. The peaking observed in the passband is a typical second order (2-pole) response transfer function. This peaking is caused by reduced phase-margin. In an ideal second order function, 3dB of peaking is the result of a damping ratio of about 0.4 which corresponds to a phase-margin of 45°.

To observe the effect of stray shunting capacitance of the feedback resistor on the response, a new circuit model was made (Fig. 5.2 inset) in which noise was neglected, but G_F, the feedback conductance was replaced by a two-port network including "C_{SH}". Also in this model the input (A_1) amplifier was modeled explicitly. To write the transimpedance of this model would be exceedingly tedious since four nodes are involved. This task is simplified by the powerful software in our APL time-shared computer. The Admittance Matrix (A-Matrix) of the circuit without feedback was written and the A-Matrix of the feedback network was also written. These matricies were entered into a circuit analysis program on this computer which is capable of combining the matricies to yield the A-Matrix of the closed-loop feedback circuit. The transimpedance of this circuit is then simply the A_{21} term of the new A-Matrix. The magnitude of this term plotted against frequency for a suitable set of parameters ($C_F = 1 \times 10^{-15}$, $C_{SH} = 1 \times 10^{-15}$) is shown in Fig. 5.2. In Fig. 5.2(a) it was assumed that the feedback capacitance of (A_1) as well as stray capacitance from gate to ground is zero, while in Fig. 5.2(b) $C_{stray} = 0.37$ pf, and the feedback capacitance of A_1, $C_{GD} = 0.13$ pf. The results of 5.2(b) compare quite closely to the actual measurements on receiver #3 shown in Fig. 5.1. In receiver #1,

Receiver	Voltage Gain	f-3dB of Voltage Gain Section	Amplifier Input Capacitance	e_n $V/\sqrt{Hz}$	RF Ω	Open Loop f-3dB	APD Dark current at bias	APD Capacitance at bias	Closed Loop f-3dB
1	380	$9x10^6$	5pf	$5x10^{-9}$	$6.12x10^6$	42KHz	$8x10^{-10}$A@10V	0.3pf @10V	6.9MHz
2	390	$8x10^6$	2pf	$22x10^{-9}$	$19.6x10^6$	25KHz		0.3pf @10V	
3	250	$8.5x10^6$	2pf	$22x10^{-9}$	$12.4x10^6$	32KHz	$4.85x10^{-8}$ A@12V	1.5pf @10V	6.35MHz

TABLE 3

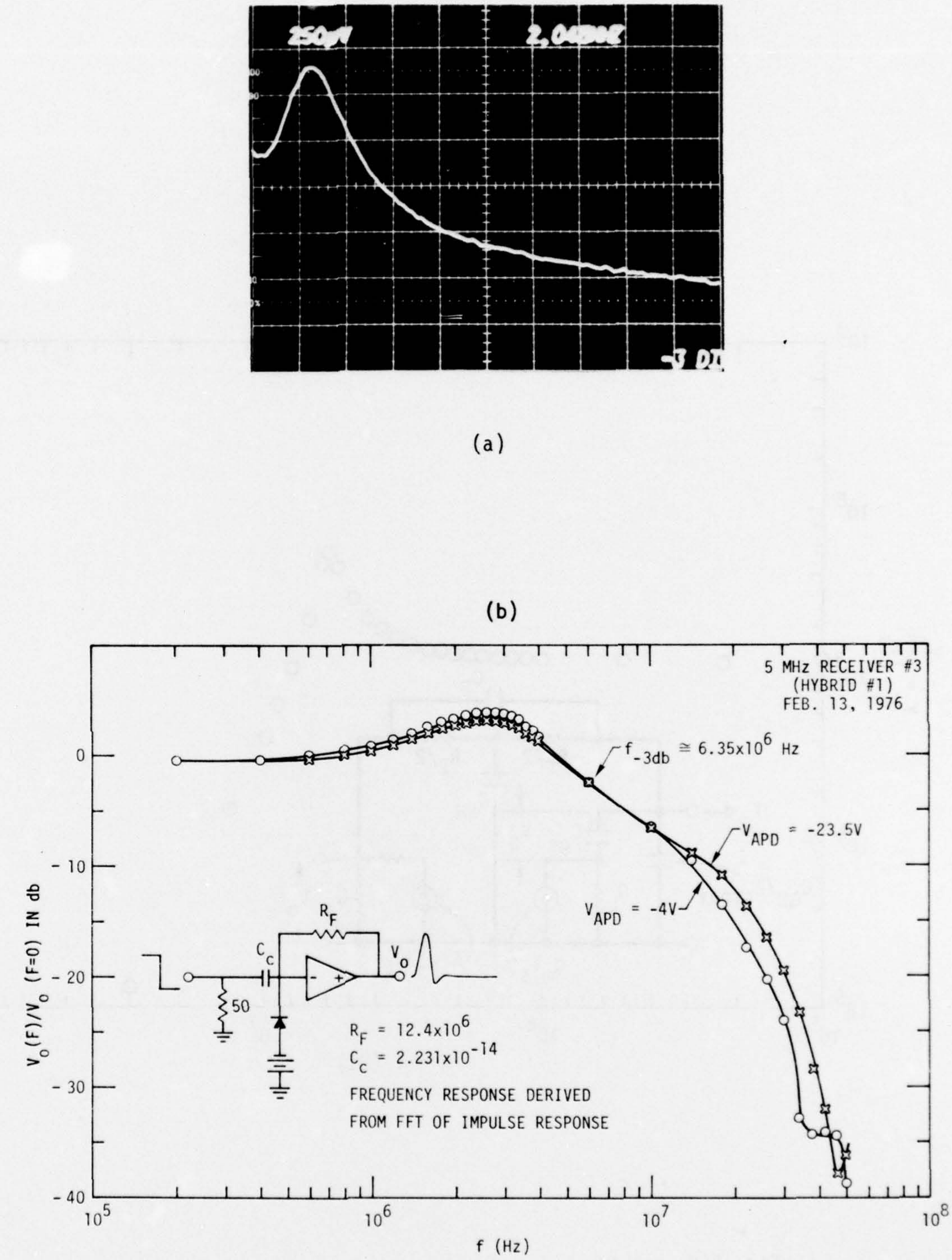

(a)

(b)

Fig. 5.1. Measured amplitude vs. frequency response for receiver #3 as determined by taking FFT of the impulse response. (a) Direct output of the DPO on linear axes and (b) corrected to logarithmic axes.

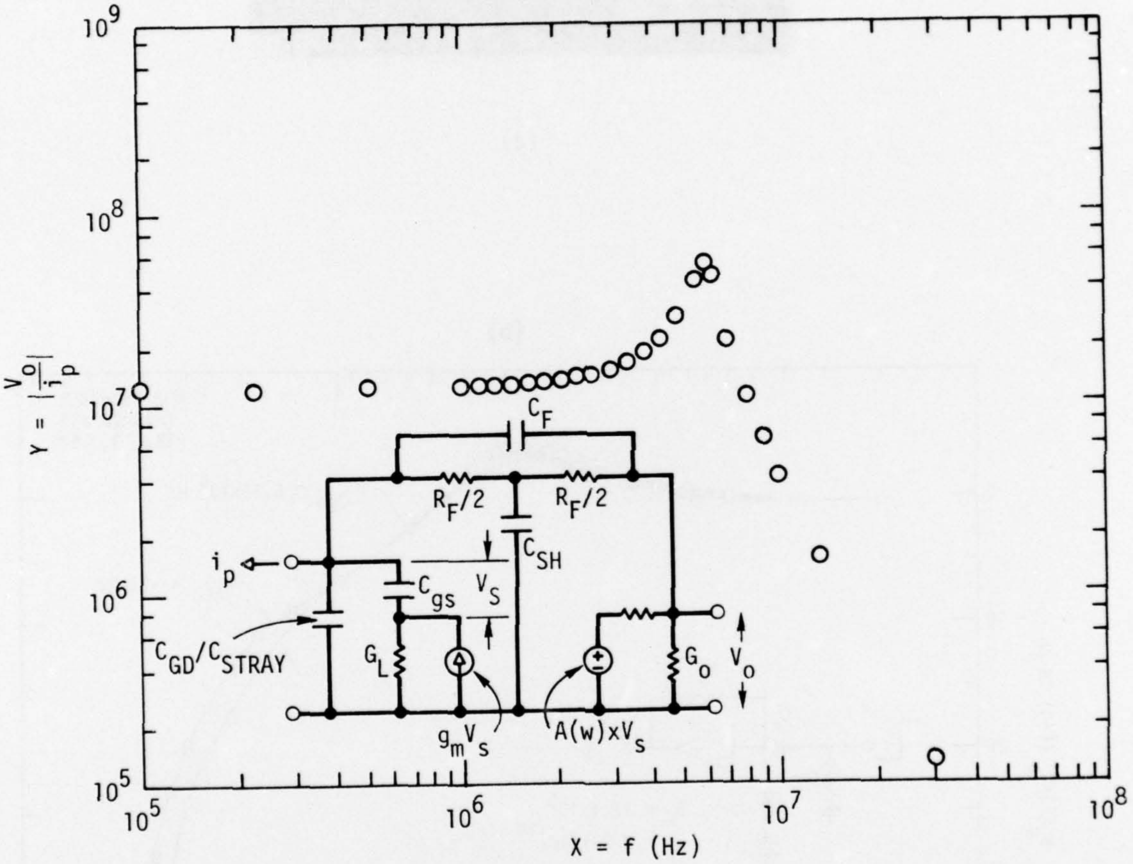

Fig. 5.2. a) Circuit model showing peaking in the passband.

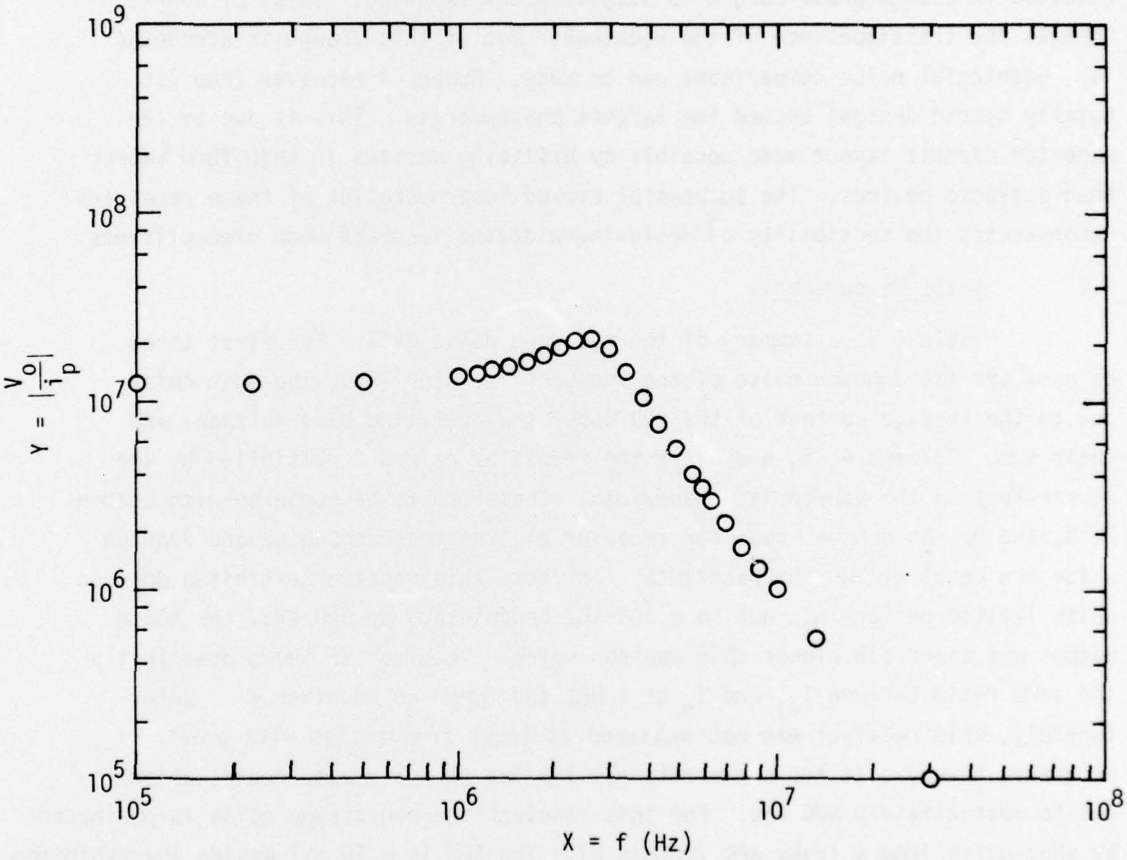

Fig. 5.2 b) Magnitude of transimpedance of Receiver #3 vs. frequency.

the phase margin was so small that oscillation took place in the closed-loop condition. In order to use that receiver for noise measurements, the feedback voltage was divided by two. This was the easiest thing to do at the time and resulted in enough phase-margin to stabilize the response. This, of course, changes the transimpedance of the receiver. But if this change is accounted for, meaningful noise comparisons can be made. Number 3 receiver (the 1st totally hybrid design) showed the largest phase-margin. This is due to the superior circuit layout made possible by utilizing devices in chip form rather than packaged devices. The successful closed-loop operation of these receivers demonstrates the feasibility of designing wideband feedback mode preamplifiers.

5.2 Noise Measurements

Table 4 is a summary of the measured noise data. The first three columns are the Johnson noise of the feedback resistor (R_F), the shot noise due to the leakage current of the APD under the operating bias voltage, and their sum. Columns 4, 5, and 6 are the result of column 3 multiplied by the square root of the appropriate bandwidth. These are to be compared with columns 7, 8, and 9. As can be seen, for receiver #1, the measured noise and Johnson noise are equal at 100 KHz bandwidth. In fact, this receiver exhibited Johnson noise limited performance out to a 300 KHz bandwidth. By 500 KHz, the noise output was about 3dB higher than Johnson noise. Receiver #3 shows practically the same ratio between i_{nj} and i_n at 1 MHz and 5 MHz as receiver #1. Unfortunately, this receiver was not measured at lower frequencies with great accuracy, however, it too shows response limited by non-preamp contributions out to approximately 500 KHz. For this receiver the non-preamp noise is dominated by shot-noise from a leaky APD (column 2). The APD is a 10 mil device and exhibited acceptable leakage when it was installed, but the surface passivation was subsequently damaged resulting in an order of magnitude increase in dark current. The performance of receiver #2 is anomalous and the noise voltage output even at 100 KHz was 7dB higher than expected. Much more can be learned about the receiver performance by studying the shape of the output noise voltage ($\simeq i_n/R_o$) vs. frequency.

	EXPECTED NOISE CURRENT DENSITIES			EXPECTED TOTAL i_n			MEASURED i_n DUE TO SHOT, THERMAL, PREAMP			MEASURED $V_n (\propto i_n R_o)$	
RCVR	i_{nj} $A/\sqrt{Hz}$	i_{ns} $A/\sqrt{Hz}$	$i_n = \sqrt{i_{nj}^2 + i_{ns}^2}$ $A/\sqrt{Hz}$	ΔF=100kHz A	1 MHz A	5 MHz A	100 kHz A	1 MHz A	5 MHz A	1 MHz mV	5 MHz mV
1	5.159×10^{-14}	2.2×10^{-14}	5.2×10^{-14}	1.12×10^{-11}	5.2×10^{-11}	11.2×10^{-11}	$\sim 1 \times 10^{-11}$	8.9×10^{-11}	44.4×10^{-11}	0.94	4.62
2	2.90×10^{-14}	1.38×10^{-14}	3.21×10^{-14}	1.01×10^{-11}	3.21×10^{-11}	7.18×10^{-11}	2.3×10^{-11}	29.1×10^{-11}	72.5×10^{-11}	5.7	14.2
3	3.625×10^{-14}	15.89×10^{-14}	16.3×10^{-14}	5.15×10^{-11}	16.3×10^{-11}	36.4×10^{-11}	3.83×10^{-11}	20.2×10^{-11}	107×10^{-11}	0.4	2.12

TABLE 4

Figs. 5.3 and 5.4 are plots of measured noise output vs. frequency for receiver #1 and #3. Receiver #1 data was measured with the output filtered by a 6-pole Butterworth lowpass filter which had 3dB frequency at 5 MHz and a roll-off rate of 37dB/octave. Receiver #3 data is shown unfiltered. The peak at 20 MHz is not of concern since it lies considerably outside the frequency range of interest. Also this receiver showed peaking in the passband which contributes to the magnitude of the noise response from about 1 to 5 MHz. In both receivers, the low frequency noise is the theoretically predicted values determined by shot noise and Johnson noise present at the input of the preamp. In receiver #1, the average noise in a 5 MHz bandwidth is within a factor of 3 of the Johnson noise, i.e. it is within a factor of 3 of the best that can be achieved without avalanche gain for this receiver. The NEP in a 1 MHz bandwidth was 4 times better in receiver #1 than in receiver #3. This is partially explained by the fact that receiver #3 had a very leaky photodiode with a relatively large area (10 mil dia vs. 3 mil for receiver #1). This increased area resulted in a much larger capacitance. The SD-200 input device in this receiver has $e_n = 22$ nv/$\sqrt{\text{Hz}}$ and $C_{gs} = 2$ pf. The 3N204 Mosfet used in receiver #1 has $e_n = 5$ nv/$\sqrt{\text{nz}}$ and $C_{gs} = 5$ pf.

As mentioned before, the functional relationship of the noise voltage vs. frequency is expected to vary as $e_n C_i \omega$, i.e. linearly proportional to frequency, and the effect, on the noise output, of e_n and C_i is expected to be somewhat interchangeable.

The precise dependence of the noise on these parameters must be determined by a noise model of the receiver whose predictions can be compared with the measured data. This work is in progress under a separate contract supported by the Air Force (F33615-76-C-1001).

5.3 Comparison of III-V APD Receiver Sensitivity with S-1 Photomultiplier and with Silicon APD Receiver

Receiver #1 was compared directly with an ITT S-1 photomultiplier selected for $\eta_{1.06\mu} = 0.1\%$ and a GE "laser-eye" silicon avalanche photodiode/50Ω preamp combination. Table 5 shows the results of this comparison.

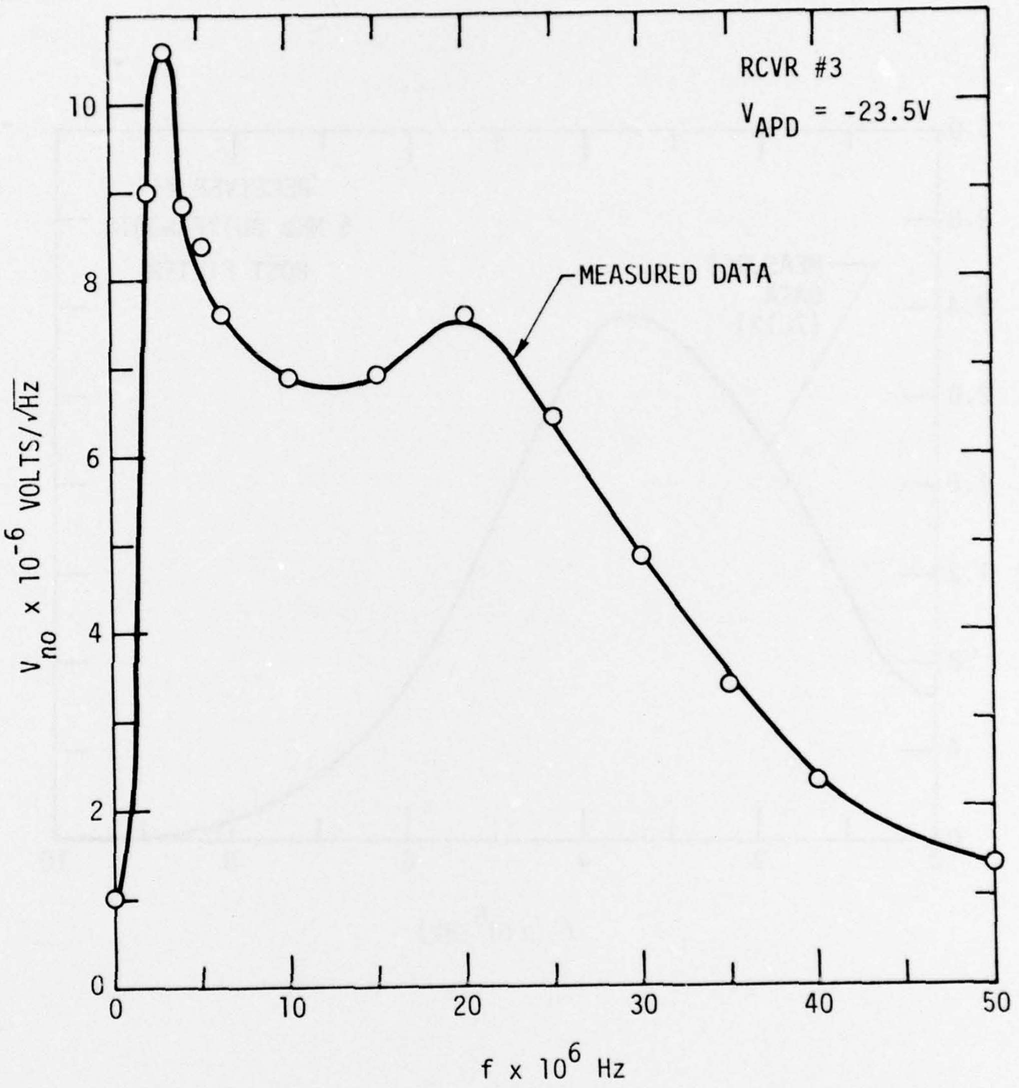

Fig. 5.3 Measured output noise voltage spectral density vs. frequency for receiver #3

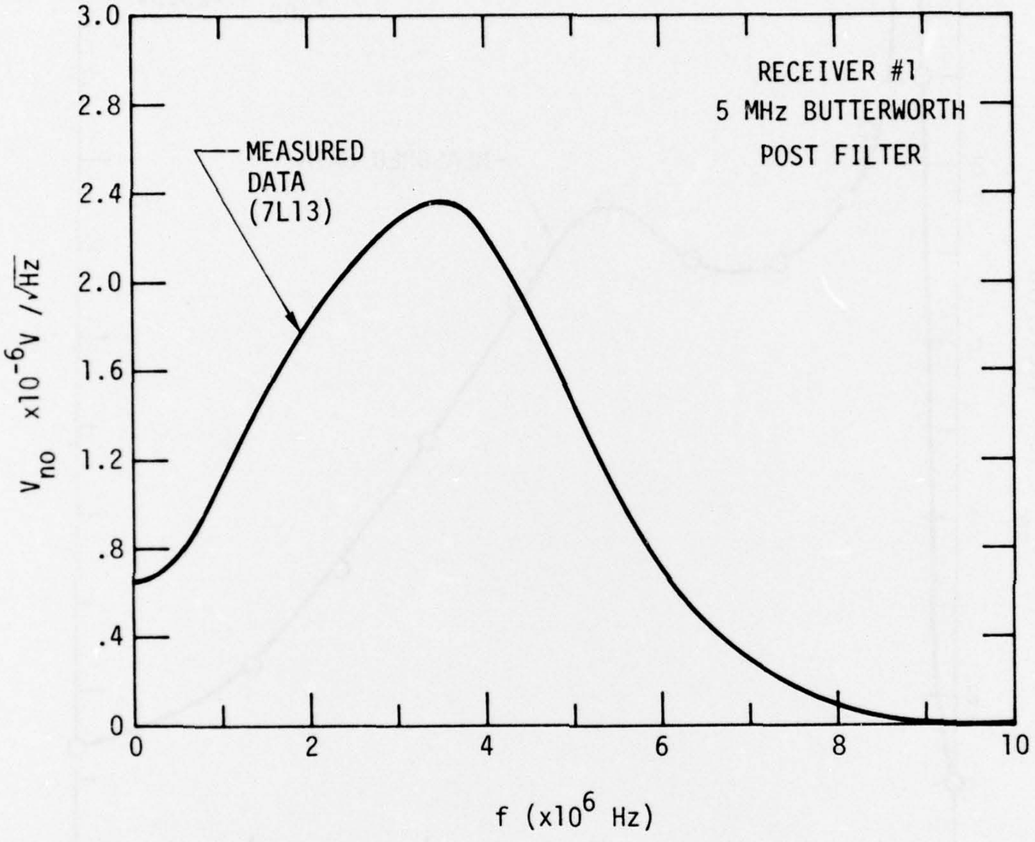

Fig. 5.4 Measured output noise voltage spectral density vs. frequency for receiver #1 with 5 MHz post filter

	Dark NEP in 1MHz Bandwidth $W\sqrt{HZ}$	NEP With Light $W\sqrt{HZ}$	
ITT S-1 Photomultiplier	$2.2x10^{-12}$	$4x10^{-12}$ (P_1=11.5 nW)	
GE Silicon APD/50Ω preamp receiver	$2x10^{-13}$	$7.5x10^{-13}$ (P_1=25 nW)	
Science Center GaAsSb photodiode receiver	$9.2x10^{-14}$	$1.16x10^{-13}$ P_1=11.5 nW	$2.3x10^{-13}$ P_1=25 nW

TABLE 5

It must be kept in mind that the performance of the GaAsSb receiver is better despite the fact that the photodiode in this receiver was not operated with avalanche gain, while both the other detectors were operated with internal gain. The measurement with and without light shining on the detectors indicated that under typical system operating conditions, the GaAsSb receiver tested would have about 35 times better signal-to-noise ratio than the S-1. The GE silicon avalanche photodiode was a selected device with manufacturer's stated quantum efficiency at 1.06μ of 30%. This device obtains its quantum efficiency by virtue of an extremely wide depletion region. This is necessary since the optical absorption depth of 1.06μ light in silicon is 0.1 cm, as compared to 10^{-4} cm in GaAsSb. Such a wide depletion width in the silicon detector necessitates the use of about 2500 volts for bias. This wide depletion width, of course, limits the ultimate frequency response of this detector due to the long transit time. While the noise performance of the silicon APD receiver was good, the measurement of dark NEP and NEP with light showed that under typical operating light levels for the system application, the GaAsSb receiver is better by a factor of between 2.2 and 3.3.

6.0 CONCLUSION

The comparison of the last section is quite impressive, considering that the "rivals" to the GaAsSb receiver are the result of refined technologies and the GaAsSb receiver was operated without avalanche gain. This comparison is indicative of the promise that the III-V alloy APD receiver has for solving the laser line-scan and related system problems.

From the work reported here, it can be concluded that the crucial receiver parameters limiting the receiver performance are the quantum efficiency, η; the avalanche gain, M; the detector dark current, I_D; the avalanche gain excess noise multiplier, x_n; the total equivalent input capacitance appearing at the input of the preamp C_i, and the equivalent input noise voltage spectral density of the first stage of the preamp, e_n. With a given η, the best performance is obtained by operating with enough avalanche gain for the shot noise to exceed the other noise sources. The limit of how much avalanche gain can be used is in turn set by the magnitude of x_n. C_i and e_n together determine the performance in the absence of avalanche gain and influence the performance when avalanche gain is present. In fact with a sufficiently low noise, low capacitance preamplifier, it is possible to meet the system requirements without avalanche gain.

Our first attempt at this problem resulted in a receiver which can meet the system requirements with between 3.3 and 4.4 nW of incident radiation. This was done without avalanche gain and with possibly not the optimum choice for the first stage of the preamp.

There are two device areas where advances will improve the system performance. One is the device used as the first stage of the preamp, the other is improvements in the avalanche photodiode. Of these the latter seems closest to fruitful results.

Overall, we have developed a promising technology for wide-band, sensitive detection of 1.06μm radiation. We feel that this technology is capable of substantial improvement in the near term and deserves continued support.

7.0 REFERENCES

1. R. C. Eden, "Heterojunction III-V Alloy Photodetectors for High Sensitivity 1.06μ Optical Receivers," Proc. IEEE, **63**, #1, Jan 1975.
2. T. P. Pearsall, Private Communication and T. P. Pearsall, R. E. Nahory, and M. A. Pollack in 1975 Device Resarch Conference (Ottawa) paper.
3. G. A. Antypas and L. W. James, J. Appl. Phys. **41**, 2165 (1970).
4. M. B. Panish and M. Ilegems, *Progress in Solid State Chemistry*, ed. by H. Reiss and J. McCaldin (Pergamon Press, New York,) **7**, 39 (1972).
5. G. D. Robinson, "Properties of Thin Film Electron-Beam Vacuum-Deposited Cermet Resistors," paper presented at 1967 AVS Symposium on Thin Film Technology (Anaheim, California).
6. M. B. Thomas, W. M. Coderre and J. C. Woolley, Phys. Stat. Sol. **A2**, k 141 (1970).
7. G. H. Olsen and M. Ettenberg, J. Appl. Phys. **45**, 5112 (1974).

☆ U. S. GOVERNMENT PRINTING OFFICE: 1976 — 757-001/59

DA
FIL
2-